Effect of surface orientation on dissolution rate and surface dynamics of UO2 single crystals in nitric acid

Solène Bertolotto, Stephanie Szenknect, Sophie Lalleman, Alastair Magnaldo, Philippe Raison, Michaël Odorico, Renaud Podor, Laurent Claparede, Nicolas Dacheux

Journal Pre-proof

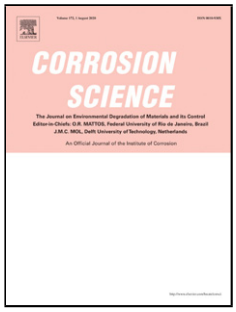

Effect of surface orientation on dissolution rate and surface dynamics of UO_2 single crystals in nitric acid

Solène Bertolotto (Conceptualization) (Data curation) (Formal analysis) (Investigation) (Methodology) (Writing - original draft), Stéphanie Szenknect (Conceptualization) (Supervision) (Validation) (Writing - original draft) (Writing - review and editing), Sophie Lalleman (Conceptualization) (Validation) (Supervision) (Writing - review and editing), Alastair Magnaldo (Conceptualization) (Formal analysis) (Validation) (Writing - review and editing), Philippe Raison (Investigation) (Methodology) (Writing - review and editing), Michael Odorico (Investigation) (Methodology) (Data curation), Renaud Podor (Investigation) (Methodology), Laurent Claparede (Supervision), Nicolas Dacheux (Conceptualization) (Validation) (Supervision) (Writing - review and editing)

PII: S0010-938X(20)31395-0

DOI: https://doi.org/10.1016/j.corsci.2020.109020

Reference: CS 109020

To appear in: *Corrosion Science*

Received Date: 12 June 2020

Revised Date: 15 September 2020

Accepted Date: 18 September 2020

Please cite this article as: { doi: https://doi.org/

Effect of surface orientation on dissolution rate and surface dynamics of UO_2 single crystals in nitric acid.

Solène Bertolotto[a,b], Stéphanie Szenknect[b,*], Sophie Lalleman[a], Alastair Magnaldo[a], Philippe Raison[c], Michael Odorico[b], Renaud Podor[b], Laurent Claparede[b], Nicolas Dacheux[b]

a: CEA, DEN, DMRC, Univ Montpellier, Marcoule, France
b: ICSM, Univ Montpellier, CEA, CNRS, ENSCM, Marcoule, Bagnols sur Cèze, France
c: European Commission, Joint Research Centre-JRC, Karlsruhe, Germany
*corresponding author: stephanie.szenknect@cea.fr

Graphical Abstract

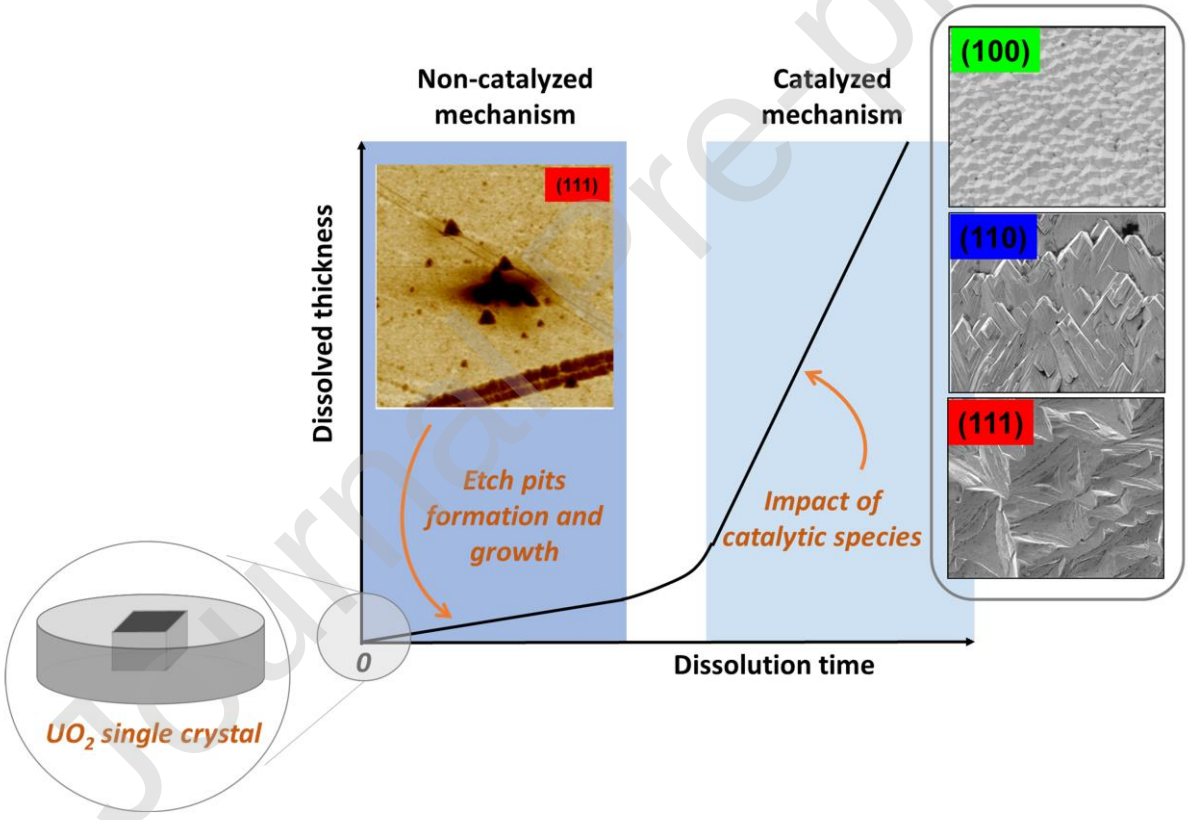

Highlights

- UO_2 single crystals with (100), (110) and (111) surfaces were dissolved in 2 M HNO_3.
- Two successive kinetic regimes were identified during dissolution.
- The impact of the initial surface orientation on the dissolution rate was evaluated.

- During the first kinetic regime, the dissolution occurred mainly at surface defect sites.
- The second kinetic step was attributed to a catalysed dissolution mechanism.
- Catalytic species were produced at the solid/solution interface during the first step.

Abstract

UO_2 single crystals with (100), (110) and (111) oriented faces were dissolved in 2 $mol.L^{-1}$ HNO_3 at room temperature. The evolution of the topography of the surface was monitored and reliable dissolution rates corresponding to the three crystallographic orientations were determined under controlled hydrodynamic and chemical conditions. The dissolution tests of UO_2 polished single crystals showed two different kinetic steps. During the first uncatalysed kinetic regime, the enhanced reactivity of the surface at defect sites was demonstrated. The second kinetic step was attributed to a catalysed dissolution mechanism involving species produced at the solid/solution interface during the first step.

Keywords

A. TYPES OF MATERIAL: Acid solutions, ceramic
B. TECHNIQUES: SEM, AFM, XRD, ICP-OES, ICP-MS
C. PROPERTIES AND PHENOMENA: Acid corrosion, pitting corrosion, kinetic parameters

1. Introduction

Currently in France where reprocessing is part of the nuclear fuel cycle, most of nuclear fuels are composed of enriched uranium-based UO_2 pellets, in which about 3.5 to 5 % of uranium atoms are present as fissile ^{235}U isotope. UO_2 pellets are dense (95 % TD) and polycrystalline ceramic. During its stay for 3 to 5 years in the reactor, the ceramic is submitted to neutron absorption and fission of several isotopes, such as ^{235}U , ^{239}Pu and ^{241}Pu, leading to the formation of a large variety of fission products. In France, spent nuclear fuels (SNF) are recycled in order to recover reusable uranium and plutonium. The head step of the reprocessing process deals with the dissolution of the SNF in hot concentrated nitric acid. The SNF material is heterogeneous in terms of microstructure (cracks, porosity), elementary composition (fission and transmutation products) and distribution (enriched Pu zones) [1-4], which could significantly influence the dissolution rate.

After discharging from the core, SNF is still containing about 95 % of remaining uranium and 1% of plutonium. Due to the very high specific activity of SNF, its reprocessing is often studied using unirradiated UO_2. The dissolution mechanism of UO_2 in nitric acid solutions involves the oxidation of uranium (IV) to uranium (VI) at the solid/solution interface [5, 6]. According to literature [7-11], the most likely mechanism is initiated by a redox reaction between UO_2 and HNO_3 at the solid/solution interface following reaction (1):

$$UO_2(s) + HNO_3(aq) + 2\,H^+ \rightarrow UO_2^{2+}(aq) + HNO_2(aq) + H_2O \quad (1)$$

The rate of this reaction is considered to be slow [10]. According to this reaction, the increase of the nitrous acid concentration is proportional to the concentration of uranyl nitrate in solution [9, 12]. A second reaction between UO_2 and nitrous acid is suspected to be much faster than reaction (1) [10]:

$$UO_2(s) + 2\,HNO_2(aq) + 2\,H^+ \rightarrow UO_2^{2+}\,(aq) + 2\,NO(aq) + 2H_2O \quad (2)$$

As HNO_2 is a product of reaction (1), the dissolution mechanism of UO_2 in nitric acid solutions was described as an autocatalytic reaction [13, 14]. Several studies [10, 15, 16] underlined on the one hand, the increase of the dissolution rate when adding nitrite salts to the nitric acid solutions and on the other hand, the decrease of the dissolution rate when nitrous acid scavengers, like hydrazinium ions or urea, are added to nitric acid. These results indicated that nitrous acid could be the catalytic species. However, Desigan et al. [11] observed that nitrous acid decomposed quickly to NOx gases following reaction (3):

$$2\,HNO_2(aq) \leftrightarrows NO_2(aq) + NO(aq) + H_2O \quad (3)$$

It is also important to note that the products of reaction (3) can recombine in nitric acid solutions to produce nitrous acid, according to reactions (4) and (5) [14, 16]:

$$NO_2(aq) + H_2O \leftrightarrows HNO_2(aq) + HNO_3(aq) \quad (4)$$

$$H^+ + NO_3^- + 2NO(aq) + H_2O \leftrightarrows 3\ HNO_2(aq) \quad (5)$$

Thus, even if the true nature of the catalytic species remained unknown, HNO_2 plays a key role in the autocatalytic mechanism of UO_2 dissolution in nitric acid solutions [7-9, 17, 18].

Several studies dealing with the kinetics of UO_2 dissolution in nitric acid media were conducted from decades, leading to controversial results. Inconsistencies between results reported in the literature arise mainly from two issues. First, hydrodynamics is not well controlled during the dissolution tests. Thus, dissolution rates can be controlled by diffusion processes and not by chemical reactions [10, 19]. As a direct consequence, concentrations of reactive species in the bulk solution differ from that at the solid/solution interface [17]. Secondly, UO_2 samples with various structures, such as powders, sintered pellets or single crystals were handled in dissolution experiments. Powdered samples obtained by grinding massive samples incorporate high density of defects and often show heterogeneous grain size [10, 13]. Grain boundaries, pores and cracks present at the surface of the pellet are known to be preferential zones of dissolution [13, 20-24]. Even for a single crystal, the spatial distribution of the surface reactivity has been evidenced by dissolution studies [25]. These various observations led to the conclusions that powders, pellets and single crystals exhibit different surface densities of reactive sites, and that the spatial distribution of the reactive sites is heterogeneous and generally unknown. Thus, even if dissolution rate is normalised by the surface area, the values obtained using UO_2 samples of various structures can differ strongly.

Finally, the comparison of UO_2 dissolution rates is complicated by the sharp change in the dissolution kinetics, when moving from uncatalysed reaction (1) to catalysed reaction (2). The poor control of hydrodynamics associated to the existence of topographic defects at the interface between UO_2 and nitric acid solution influences the rate of production of catalytic species, and thus modifies drastically the overall dissolution rate. In view of these difficulties, micrometric single crystals appear as the simplest interface to obtain reliable dissolution rates of UO_2 in nitric acid media. From a geometric point of view, oriented and polished single crystal presents large and flat solid/solution interface. This interface can be considered as free of steps, pores, grain boundaries or cracks, which allows to manage properly hydrodynamic conditions in both catalysed and uncatalysed regimes.

Moreover, the use of oriented single crystals makes it possible to evaluate the impact of surface orientation on the dissolution rate. Uranium dioxide crystallizes with a fluorite type-structure (spatial group $Fm\bar{3}m$). The lattice is composed of uranium atoms (+IV) organized in

a face-centred cubic structure and oxygen atoms (-II) fill every tetrahedral sites of the lattice (eight sites). This specific spatial group owns two mirrors symmetries and one axial symmetry. A combination of these three symmetric operations allows (100), (110) and (111) planes to recur in all directions and finally to build the UO_2 structure. The stability of oriented faces and the contribution of defects have been investigated in the literature for fluorite-type materials such as CaF_2 and CeO_2 [22, 23, 26-28]. (111) oriented surface seems to be the most resistant to dissolution. It is worth noting that dissolution kinetics of CaF_2 and CeO_2 is not controlled by an oxidative process as for UO_2 in nitric acid. Nevertheless, a recent study of the dissolution under irradiation of UO_2 thin films [29] showed that unlike (100) and (110), the (111) oriented surface stopped dissolving after one minute under irradiation. This result suggests that the (111) UO_2 surface is the most resistant to radiolytic dissolution.

In this work, single crystals with (100), (110) and (111) oriented faces were dissolved in nitric acid solution. The evolution of the topography of the surface was monitored and dissolution rates corresponding to the three crystallographic orientations were determined under controlled hydrodynamic conditions. Specific dissolution tests were performed for the (111) oriented surface. First, the topographic evolution of the interface was monitored by AFM at the beginning of the dissolution reaction in order to evidence the role of defects during the catalysed kinetic regime. Secondly, catalysed conditions were maintained in order to determine reliable dissolution rate under controlled hydrodynamic and chemical conditions.

2. Material and Methods

2.1. Preparation of UO_2 polished single crystals and surface characterizations

Macroscopic single crystals of UO_2 were recovered a long time ago from a melted core of depleted UO_2 in a research reactor. Many years after, smaller single crystals were cut and oriented at the Joined Research Centre of Karlsruhe thanks to Laue diffraction method in order to produce the millimeter-sized samples used in this work. Single crystals were oriented and cut along to (100), (110) and (111) planes. The three oriented surfaces are represented in **Fig. 1**. They reveal different arrangements of U and O atoms. Surfaces (100) and (111) are formed of alternating planes only composed of uranium or oxygen atoms, such as -O-U-O- planes for the (100) surface and $-O_2$-U-O_2-U-O_2- planes for the (111) surface. On the contrary, each atomic plane of the (110) surface is composed of U and O atoms. The (100) surface is the only polar surface among all the others.

The oriented samples obtained by cutting single crystals have an irregular slab form. The samples were weighted and their dimensions determined thanks to an optical macroscope. The surface area of the main oriented face was determined by using the image

processing software ImageJ. The pixel size was calibrated at the appropriate magnification. After binarization of the whole sample image, the surface area of the black pixels, which corresponds to the geometric surface area of the oriented face was determined. The geometric properties of the samples are gathered in **Table 1**. In order to expose a single oriented surface to the solution, samples were embedded in an epoxy resin (EpoFix, Struers). Then, samples were polished to remove completely the resin from the surface exposed to the dissolution medium. Several polishing discs were used, the last one was used with 1 µm diamond suspension during 1 min with rotation at 200 rpm. The final polishing step was performed with colloidal silica (30 sec with rotation at 200 rpm).

The orientation of the surface was controlled after mechanical polishing by X-Rays Diffraction (XRD). XRD patterns were collected using a Bruker D8-Advance diffractometer (LynxEye detector) in the reflection geometry with Cu-$K_{\alpha 1.2}$ radiation (λ = 1.5418 Å). The analyses were carried out at room temperature in an angular range of $10° < 2\theta < 100°$, with a step of 0.026° and a total counting time of about 2 h. XRD patterns of the three oriented faces and of UO_2 powder used as a reference are presented in **Fig. 2.**

The XRD diagrams of each sample presented only XRD peaks of the UO_2 lattice, without any additional phase. The unit cell parameter was evaluated to 5.469(4) Å as the average of the values obtained by the refinement of each diagram. It was in agreement with the value determined by Leinders et al. [30] for stoichiometric UO_2 (a = 5.47127(8) Å). In addition, only the XRD lines corresponding to the expected orientation were observed. From the XRD patterns analysis, it was assumed that the polishing step did not strongly modify the orientation of the surface of single crystals exposed to solution. The specific shape of the XRD peaks obtained for the single crystals was attributed to two phenomena. The first one is the “flat plate” phenomenon, which is a well-known artefact for XRD analysis of massive samples. The second one is the “mosaic structure” phenomenon. Indeed, in a real crystal, the lattice is broken up in several tiny blocks having a size around 1000 Å. Each block is slightly disoriented one from another. The disorientation angle is small but at worst, it can reached 1°. For a disorientation angle of ε, each block can diffract in a range between the incident angle θ and $\theta + \varepsilon$ [31].

The topography of each sample was observed before dissolution experiment by Scanning Electron Microscopy (SEM, FEI Quanta 200) and by Atomic Force Microscopy (AFM, MULTIMODE 8 AFM). For SEM, a secondary electron detector (SE) and a backscattered electron detector (BSE) in vacuum conditions were used with an acceleration voltage of 30 kV. The AFM device presented an optimal vertical resolution of 1 Å and a lateral resolution of approximately 8 nm. It was outfitted with a Nanoscope 5 controller from Bruker Germany. Under dry conditions, the peak mode force was applied using SNL tips (silicon tip on silicon

nitride cantilever) from Bruker Company to perform AFM imaging. The spring constant was 0.35 $N.m^{-1}$. This mode was used with specific surface texture parameters defined by the operator in order to minimize the force. The average roughness of the surface, S_a (nm), the maximum height of the surface, S_z (nm) and the developed interfacial area ratio, *Sdr* (%), were determined by AFM according to the standard ISO 25178-2 [32] (**Table 1**).

$$S_a = \frac{1}{A} \times \iint_A |z(x,y)| \, dxdy \quad (6)$$

$$S_z = S_p + S_v \quad (7)$$

$$Sdr = \frac{S_{corr}^{f} - A}{A} \times 100 \quad (8)$$

where A corresponds to projected area (m^2), S_P is the height of the highest point (µm), S_v is the height of the deepest point (µm) and S_{corr}^{f} corresponds to the surface area corrected by the surface texture (m^2).

At the end of the dissolution experiments, the samples were characterized by SEM under environmental conditions with SE detector. In order to observe a large zone of each sample, twenty pictures were taken at low magnification and then stitched using the plugin Grid/collection stitching [33] of Fiji software. Then, SEM micrographs were recorded at different magnifications. For one of these magnifications, three tilted images were recorded using three different angles (-10°; 0°; 10°) following the protocol developed by Podor et al. [34]. The stereoscopic images were then pre-aligned using the SIFT method of FIJI software [35]. 3D-reconstructions of the zone observed were obtained using the three tilted images and the commercial Alicona Mex software. A reference plane cutting the 3D-recontruction was defined: its z-position was determined in order to equitably distribute matter above and below it. From the 3D-reconstruction, surface texture or topographic parameters such as the maximum height difference (S_Z in µm), the average arithmetic roughness (S_a in µm) and the developed interfacial area ratio, (*Sdr* in %) were also calculated at the end of the dissolution experiment. The topographic parameters were calculated as the average of the results obtained from 3D-recontructions of three different zones at the surface of the sample.

A representative SEM image of each oriented surface obtained with SE detector is presented in **Fig. 3 (a-c)**. SE detector is sensitive to topographic contrast. The micrographs reported in **Fig. 3 (a-c)** confirmed that the polished surface was smooth without any deep scratches. The BSE detector was used to perform Electron Channeling Contrast Imaging (ECCI). This technique allowed the observation and characterization of extended crystalline defects such as dislocations [36-40]. Numerous white lines were observed, which were attributed to the presence of defects (**Fig. 3 (2a-c)**) [41]. This observation was made for the three oriented samples. The observation of UO_2 single crystals by SEM-ECCI has been already

reported in few studies [39] but was not associated to AFM images. In this work, the same zone of the (110) and (111) oriented samples was also characterized by AFM (**Fig. 3 (b-c)**). A perfect match existed between the positions of the white lines evidenced by SEM-ECCI and the nanometer dents detected by AFM. Thus, thanks to high vertical resolution provided by AFM, tiny height variations were detected that corresponded either to polishing scratches of few nanometers in depth or to extended defects such as dislocations lines and loops.

2.2. Dissolution experiments

Dissolution experiments under standard conditions

The dissolution tests were performed at room temperature under static conditions and mechanical stirring, using 240 mL PTFE reactors. Three oriented single crystals were put in 2 mol.L^{-1} HNO_3 solution for 35 days. The total volume of solution was 200 mL. At regular times, 5 mL of solution were sampled and replaced by the same volume of fresh nitric acid to maintain a constant volume of solution in contact with the crystal. After dilution with 0.2 mol.L^{-1} HNO_3 solution, the elemental uranium concentration was measured using Inductively-Coupled Plasma Mass Spectrometry (ICP-MS, Thermo Fisher). ICP-MS was calibrated using several standard solutions prepared by dilution of a certified standard solution at 1000 ppm in uranium using 0.2 mol.L^{-1} HNO_3 solution. Additionally, ^{193}Ir and ^{209}Bi were used as internal standards. The elemental uranium concentration was calculated as the average of three replicates. In these conditions, the detection limit for uranium reached 0.1 ppb (i.e. 4.2×10^{-10} mol.L^{-1}).

Dissolution experiment under controlled catalysed conditions

In order to perform dissolution tests in catalytic conditions, copper chips (VWR chemicals) were dissolved in aerated nitric acid. Then, this solution was used to dissolve UO_2 (111)- ② single crystal. Cu has been already used to simulate UO_2 dissolution in nitric acid [14, 19, 42]. The reaction is similar, as it is also autocatalytic and produces NO_x and nitrous acid [43]. Indeed, in aerated and concentrated nitric acid solutions, Turnbull et al. [44, 45] demonstrated that the key role of oxygen was to produce cuprous ions, which catalyzed the reduction of nitrate to nitrite ions. The cupric ions formed by the former reduction reaction reacted with copper in a catalytic cycle to reproduce cuprous ions. In concentrated nitric acid solution, the solubility of the passivating corrosion products is high and the catalytic cycle is maintained until copper is completely dissolved as Cu(II). It could be argued that Cu(II) can support the corrosion of UO_2 leading to the production of Cu(I). Then, in aerated nitric acid solutions, Cu(I) is likely to undergo oxidation to Cu(II). However, Charlier et al. [14] compared dissolution rates of UO_2 particles in solutions loaded with species produced by dissolving the

same molar quantity of copper or uranium dioxide. For the same experimental conditions, they obtained the same dissolution rate of UO_2. This result demonstrated that the rate of dissolution of UO_2 was controlled by the amount of nitrous acid or NOx in the prepared solution and was independent on the Cu(II) concentration. In this work, Cu was preferred to UO_2 to prepare the solution loaded with the catalytic species, because the dissolution rate of UO_2 single crystals was determined by analyses of the uranium elemental concentration in solution. The concentration of uranium produced by the dissolution of the single crystals was several orders of magnitude lower than the concentration of uranium in the loaded solution (i.e $\sim 10^{-2}$ mol.L^{-1}). Thus, it was virtually impossible to detect the very low increase of the uranium elemental concentration caused by the dissolution of single crystals in the loaded solution and then, to determine accurate dissolution rates.

The amount of catalytic species produced in solution (C_Z expressed in mol.L^{-1}) depends on the mass of copper dissolved. It was estimated using the mass balance equation (9) [19, 42, 43] and equation (10) [13].

$$Cu_{(s)} + \frac{8}{3} HNO_{3(aq)} \rightarrow Cu(NO_3)_{2(aq)} + \frac{2}{3} NO_{(aq)} + 2\ H_2O \quad (9)$$

$$X = 1 - \frac{\mu_H \times m_{Cu}}{V_H \times C_0 \times M_{Cu}} = 1 - \frac{\mu_H \times C_Z(t)}{\mu_Z \times C_0} \quad (10)$$

where C_0 (mol.L^{-1}) is the initial nitric acid concentration; μ_H is the stoichiometric coefficient of nitric acid consumption, equal to 8/3; μ_Z is the stoichiometric coefficient of catalytic species production, equal to 1; m_{Cu} is the mass of copper dissolved (g) ; V_H is the volume of nitric acid (L) and M_{Cu} is the molar weight of copper (63.55 g.mol^{-1}).

In the dissolution test of UO_2 single crystal, X was equal to 0.96, which corresponded to 0.5 g of copper dissolved and 3×10^{-2} mol.L^{-1} of catalytic species produced. C_0 was equal to 2.08 mol.L^{-1} in order to obtain 2 mol.L^{-1} nitric acid solution after Cu dissolution. The total dissolution of Cu chips was performed in 250 mL of solution. It required 4 hours at 60 °C under mechanical stirring. After the complete dissolution of Cu, the bottle was dipped in a cold-water trap in order to quickly decrease the solution temperature to 22 °C.

Even if the catalytic species have not been definitely identified up to now, they have been systematically associated to the presence of nitrous acid and NO_X (NO and NO_2) in solution. These species are not stable in solution. To avoid their decomposition in NO_x (g) or their volatilization, and therefore to prevent the decrease of catalytic species concentration, a 2 cm thick layer of paraffin oil was deposited at the surface of the solution during the dissolution of Cu chips.

The dissolution of (111)- ② single crystal was performed at room temperature under dynamic conditions and mechanical stirring using a 25 mL PTFE reactor continuously fed with the nitric acid solution loaded with catalytic species. In order to limit the production of

radioactive liquid waste and to minimize the mass of solid over the volume of solution ratio, the nitric acid solution was recycled. The total volume of solution including the reactor, the bottle for the solution supply and the tubes, reached 250 mL. The flow rate was fixed to 30 $mL.h^{-1}$ in order to minimize the thickness of the diffusion layer at the solid/solution interface. (111)- ② oriented single crystal was put in 2 $mol.L^{-1}$ HNO_3 solution loaded with the catalytic species for about 4 days. After this period, the concentration of HNO_2 in solution decreased by 25%. The conditions of the dissolution experiment varied too much and the experiment was stopped.

At regular times, 4 mL of solution were sampled and not replaced. Each aliquot was divided in two 2 mL-samples in order to perform the analyses of uranium and nitrous acid concentrations. The elemental uranium concentration was measured using ICP-MS following the same protocol as for dissolution tests performed under standard conditions. Nitrous acid was considered in this work as a tracer of the catalytic dissolution of UO_2. The evolution of the nitrous acid concentration was determined by UV-visible spectroscopy following the Griess method. First, 1 mL of 8 $mol.L^{-1}$ NaOH solution was added to the 2 mL sample in order to stabilize nitrous acid as nitrite ions and to avoid interference with uranyl ions in the UV-visible spectrum. After centrifugation of the U(VI) precipitate, 0.1 $mol.L^{-1}$ H_2SO_4 was added to the supernatant until the pH was equal to 2. Then, the colorimetric reagent was added (Nitrite Test Spectroquant®, Merck). Using the Griess method, the presence of nitrite ions induced a large non-interfered absorption band at 540 nm. Quantitative analyses were made possible by calibrating the UV-visible spectrometer using NO_2^- standard solutions prepared by dilutions of a certified NIST $NaNO_2$ standard solution at 0.1 $mol.L^{-1}$ (CertiPur® Merck).

3. Calculation

From ICP-MS analyses, the evolution of the elemental concentration, $C_U(t)$ ($g.L^{-1}$) was determined. The dissolved mass of UO_2, $\Delta m(t)$ (g) was then calculated according to the following equation:

$$\Delta m(t) = \frac{m_U(t)}{f_U} = \frac{C_U(t) \times V}{f_U} \quad (11)$$

where $m_U(t)$ (g) corresponds to the total amount of the uranium released in solution at a time t, V (L) is the volume of solution in contact with the solid and f_U ($g.g^{-1}$) is the mass fraction uranium in the solid.

The normalized weight loss, $N_L^{geo}(t)$ ($g.m^{-2}$), and the apparent dissolved thickness $e^{geo}(t)$ (µm) were calculated according to equation (12):

$$N_L^{geo}(t) = \frac{m_U(t)}{f_U \times S_{geo}} = e^{geo}(t) \times \rho \quad (12)$$

where S_{geo} (m²) is the geometric surface area of the oriented surface in contact with the solution and ρ is the density of the solid (10.96 g.cm^{-3} for UO_2).

The normalized dissolution rate of each oriented surface, $R_L^{geo}(U)$ (g.m^{-2}.d^{-1}) and the normal retreat rate $R_R^{geo}(U)$ (µm.d^{-1}) were determined using equation (13):

$$R_L^{geo}(U) = \frac{\partial N_L^{geo}(t)}{\partial t} = R_R^{geo}(U) \times \rho \quad (13)$$

Thanks to 3D surface reconstruction, the corrected surface area of the whole oriented surface at the end of the dissolution test, S_{corr}^f (m²) was determined as:

$$S_{corr}^f = \left(1 + \frac{Sdr}{100}\right) \times S_{geo} \quad (14)$$

The corrected surface area $S_{corr}(t)$ (m²) was estimated and the corrected normalized weight loss $N_L^{corr}(t)$ (g.m^{-2}) was calculated using the following equations:

$$N_L^{corr}(t) = \frac{m_U(t)}{f_U \times S_{corr}(t)} \quad (15)$$

$$\text{with } \begin{cases} S_{corr}(t) = S_{geo} \text{ for } t \le t_{ind} \\ S_{corr}(t) = a \times (t - t_{ind}) + S_{geo} \text{ for } t > t_{ind} \text{ where } a = \frac{S_{corr}^f - S_{geo}}{t_f - t_{ind}} \end{cases} \quad (16)$$

where t_{ind} (d) is the induction time defined as the dissolution time corresponding to the end of the first kinetic regime (i.e. 15 ± 1 days under standard conditions).

Finally using the corrected normalized weight loss $N_L^{corr}(t)$ in equations (12) and (13), $e^{corr}(t)$, $R_L^{corr}(U)$ and $R_R^{corr}(U)$ were calculated.

4. Results and discussion

4.1. Dissolution experiments

Macroscopic dissolution of oriented single crystals under standard conditions

In order to examine the influence of the crystallographic orientation on the dissolution of UO_2 single crystals in nitric acid media, dissolution tests were performed in 2 mol.L^{-1} HNO_3 solution at room temperature under static conditions for the three oriented surfaces (100), (110) and (111) (samples- ① in **Table 1**). The evolutions of the geometric normalized weight loss $N_L^{geo}(t)$ (g.m^{-2}) and of the dissolved mass $\Delta m(t)$ (g) obtained for each oriented UO_2 single crystal are reported in **Fig.4(a-c)**.

For the three oriented surfaces, the shape of the $N_L^{geo}(t)$ evolution was found to be similar. Mainly, two steps were observed. The first one was associated to a slow uranium

release in the solution, while the rate of uranium release increased drastically during the second step. For the three oriented surfaces, the first stage occurred for $\Delta m(t) \leq 1.6 \times 10^{-5}$ g and $C_U(t) \leq 3.5 \times 10^{-7}$ mol.L^{-1}, i.e. for a dissolution time, t_{ind} lower than 16 days. The second step started after 21 to 26 days of dissolution and was characterized by a fast and linear increase of the normalized weight loss $N_L^{geo}(t)$ or of the apparent dissolved thickness $e^{geo}(t)$. Between these two steps, a period of transition occurred, during which the normalized dissolution rate increased continuously.

The first period was called “induction time” according to the literature. A close look to the evolution of $N_L^{geo}(t)$ and $e^{geo}(t)$ during the first step showed a succession of linear increases. Nevertheless, a linear regression of $N_L^{geo}(t)$, or $e^{geo}(t)$ was made to approximate the normalized dissolution rate, $R_{L,1}^{geo}(U)$ and the normal retreat rate, $R_{R,1}^{geo}(U)$ during this step. An empirical criterion was defined to determine the end of this induction period: R^2 of the linear regression of $N_L^{geo}(t \leq t_{ind})$ higher than 0.70. The values and the associated standard errors estimated by the linear regression of the data during the first step are reported in **Table 2** for the three single crystals. The dissolution rates obtained during the first step were not significantly different for (110) and (111) oriented surfaces and slightly higher for (100). The values obtained showed that the crystal orientation did not influence strongly the dissolution rate during this induction period.

From 21- 25 days of dissolution to the end of experiment, a second kinetic step was observed. The evolution of the normalized weight loss (or of the dissolved thickness) was found to be linear (with $R^2 = 0.99$), which indicated that steady conditions were maintained and allowed the determination of constant dissolution rates $R_{L,2}^{geo}(U)$ and $R_{R,2}^{geo}(U)$ (**Table 2**). Once again, dissolution rates were not strongly influenced by the orientation of the UO_2 surface. Nevertheless, the dissolution rate determined during the second step for (111) was found to be significantly lower than that obtained for (110) and (100). The dissolution rate determined in the second step increased drastically compared to the $R_{L,1}^{geo}(U)$ estimates. For the (100) oriented surface, the dissolution rate was multiplied by a factor of 260. This factor reached 370 and 630 for (111) and (110) oriented surfaces, respectively. Such increase of the dissolution rate was already observed for polycrystalline samples of UO_2 dissolved in nitric acid media [21, 46]. It was attributed to the concomitant increases of the reactive surface area and of the concentration of catalytic species in solution. In order to distinguish the impact of these two phenomena, the topographic evolution of each oriented surface was monitored and thus, the normalized weight loss was corrected from the increase of the surface area induced by dissolution.

Topographic evolution of the oriented surfaces

After 35 days of dissolution in 2 mol.L^{-1} HNO_3 at room temperature, the samples were removed from the reactor and washed twice with deionized water. SEM images were recorded under environmental conditions with the SE detector at different magnifications (× 2,500 and × 10,000) and a series of 25 micrographs was achieved in order to obtain a large (530 × 450 µm²) SEM image (stitching) of the sample with a spatial resolution of 62 nm per pixel (**Fig. 5 (a-c)**).

The analysis of the SEM micrographs presented in **Fig. 5(a-c)** revealed different dissolution features at the surface of the three oriented samples and thus, the spatial heterogeneity of the material flux from the reacting surface. It is worth noting that the topographical observations of the oriented surfaces were made for similar weight losses (**Table 2**). For the (100) surface, SEM micrographs (**Fig. 5(a)**) revealed the formation of square-based pyramids of the same size and aligned in the same direction. The stitching of micrographs showed that pyramids covered the whole surface of the sample. (110) surface (**Fig. 5(b)**) appeared to be smoother than the other ones. Nevertheless, the micrographs recorded at the highest magnification (×10,000) showed the presence of steps, step edges having a tip form. Etch pits were hardly observed by SEM for the (100) and (110) surfaces, whereas the (111) surface (**Fig. 5(c)**) was covered by triangular etch pits. Triangular etch pits were observable with all magnifications. The size of the biggest etch pits was about 20 µm. Although macroscopic dissolution rates (**Table 2**) did not strongly depend on the crystallographic orientation of the surface exposed to nitric acid solution, the evolution of the topography was strongly influenced by the initial orientation of the solid/solution interface. The different dissolution features observed for the three oriented surfaces unveiled the heterogeneity of the surface reaction rates, which could be considered as the signature of processes occurring at the atomic scale [47].

3D reconstructions of the oriented surface allowed determining the average arithmetic roughness of the surface, S_a (nm), the maximum height difference at the surface, S_z (nm) and the developed interfacial area ratio, *Sdr* (%). These parameters were calculated for three different zones at the surface of the samples (**Fig. 6**).

The developed interfacial area ratio, *Sdr* (%), was found to vary with the orientation of the surface of UO_2. The obtained values decreased following the sequence (100) ≈ (110) > (111). Thanks to polishing, the initial value measured by AFM was estimated at 0 for all the samples (**Table 1**). At the end of the dissolution experiment, the (100) and (110) surface area increased by 39 %. For a similar mass loss or dissolved thickness, the increase of surface area

of (111) oriented surface was found to be lower (23 %). The S_a and S_z parameters increased following the sequence (100) < (110) < (111). Thus, in the direction normal to the oriented surface, the dissolution led to higher height differences for the (111) oriented surface, which is in agreement with the formation of deep corrosion pits (**Fig. 6c**). For the (100) and (110) oriented surfaces, the value of the arithmetic roughness (i.e. between 100 and 200 nm) corresponded to the mean height of the square-based pyramids and step edges, respectively.

Thanks to 3D reconstructions of the oriented surfaces, it was possible to normalize the weight loss taking into account the evolution of the corrected surface area $S_{corr}(t)$. The evolution of $N_L^{geo}(t)$ and of $N_L^{corr}(t)$ are compared in **Fig. 7**.

Despite the correction of the evolution of the surface area, the two kinetic steps were still observable (**Fig. 7(b)**). Thus, the increase of the dissolution rate observed during the second regime did not come from an increase of the surface area of the sample. The corrected normalized dissolution rate, $R_{L,2}^{corr}$ and corrected retreat rate $R_{R,2}^{corr}$ were calculated for each orientation by linear regression of the corrected normalized weight loss and of the corrected dissolved thickness, respectively. The results are summarized in **Table 2**. They showed that the macroscopic dissolution rates determined in the second kinetic regime were similar for the three oriented surfaces. Nevertheless, with a significantly lower $R_{L,2}^{corr}$ value compared to (100) and (110) surfaces, the (111) surface remained the most durable.

The production of catalytic species during a first kinetic regime has been already suspected for polycrystalline UO_2 and U-based oxides dissolved in nitric acid solutions [6-12, 15, 16, 18, 21, 48]. The same phenomenon could also explain the increase of the single crystals dissolution rate in the second regime. In order to link the two kinetic regimes observed during the dissolution of UO_2 single crystals in nitric acid solution with a specific mechanism, dedicated experiments were performed using samples with (111) oriented faces (labelled (111)- ② and (111)- ③ in **Table 1**).

Formation of etch pits at the (111) oriented surface during the first kinetic regime

Specific dissolution test was performed for the (111) oriented surface in 2 mol.L^{-1} HNO_3 at room temperature. Before the dissolution, a region of interest (ROI) with observable defects was selected at the surface of the sample (111)- ③ and height maps were obtained with AFM. The sample was removed from the reactor several times during the first kinetic step of dissolution (i.e. for $t < t_{ind}$) and was washed with deionized water before its characterization. The ROI was characterized systematically by AFM, which allowed monitoring its topographic evolution (**Fig. 8**).

After 72 hours of dissolution, the formation of triangular etch pits was evidenced. Triangles were either aligned along polishing scratches, or located at the border of the

topographic defects also observed by SEM-ECCI (**Fig.3**). After 87 hours of dissolution, each etch pit previously formed grew and new ones were formed at the border of other defects. This phenomenon was going on until the last observation made for t = 158 hours. It revealed the presence of defects, which were not easily detectable by AFM at the beginning of the experiment (for instance, scratches which were not evidenced before 87 hours of dissolution were finally covered by triangular etch pits after 134 hours). Thus, at the early stage of the dissolution, etch pits were not homogeneously distributed at the surface of the ROI. This observation was supported by the evolution of the arithmetic roughness. The initial arithmetic roughness, S_a, reached 1.8 nm and 0.2 nm, for the entire ROI and the region free from defects, respectively. After 87 hours of dissolution, S_a of the entire ROI increased up to 2.8 nm, whereas it was only 0.6 nm in region free from triangular etch pits. Finally, after 158 hours of dissolution, the S_a value was 3.7 nm and 0.7 nm for the entire ROI and the region free from triangular etch pits, respectively. Thus, the increase in the roughness of the selected ROI was mainly due to the formation of etch pits. From these images, it appeared that the pit nucleation occurred at the border of defects detected by AFM and by SEM-ECCI. These defects were thus evidenced by the presence of dents, and by electron channeling contrast with the bulk material. Regardless of the nature of these extended defects (dislocation loops, edge or screw dislocations), etch pits opened up in the vicinity.

All etch pits corresponded to equilateral triangles oriented in the same direction. The geometry and orientation of one etch pit is reported in **Fig. 9(a)** whereas the corresponding evolution of a depth profile crossing the etch pit is presented in **Fig. 9(b)**.

The edges of the equilateral triangles exhibited the specific directions $[01\bar{1}]$, $[10\bar{1}]$ and $[\bar{1}10]$ (**Fig. 9(a)**). The monitoring of the depth profiles (**Fig. 9(b)**) showed the lateral and vertical growth of etch pit. The lateral growth of etch pit (characterized by displacement of the $[\bar{1}10]$ edge) was about 10 times faster than the digging in the direction normal to the (111) surface (pay attention to the different scales in **Fig. 9(b)**). The lateral/normal length ratio of the selected etch pit was almost equal to 16 after 158 hours of dissolution, which corresponded to shallow etch pits. Moreover, the growth of etch pit in all directions seemed to slow down after 87 hours of dissolution.

The formation of similar triangular etch pits was observed for the isostructural CaF_2 but also for polycrystalline UO_2 [25, 49-52] and UO_2 single crystals [53]. This comparison indicated that even though different reaction mechanisms were involved (acid-catalysed dissolution for CaF_2 and oxidative dissolution for UO_2), the reactivity of the surface was connected to the crystallographic structure of the material. For CaF_2, Cama et al.[49] proposed that the typical triangular pit orientation was attributed to the Ca–Ca arrangements via bridging F-neighbors.

Similarly, for UO_2, such a structural control of the pit evolution at the atomic level is illustrated in **Fig. 10**.

If one layer of atoms on the (111) UO_2 plane surface is considered, the first uranium atom is randomly removed as well as its three coordinating oxygen atoms (**Fig. 10(b)**). Then, a second uranium atom can be detached randomly among the six 2-coordinated U atoms surrounding the first one (**Fig. 10(c)**). Finally, the only 1-coordinated uranium atom remaining at the surface is preferentially removed from the surface (**Fig. 10(d)**). This sequence yields to the formation of a triangular etch pit. The detachment of atoms is then laterally spreading, which leads to the growth of etch pit. As the triangles remained equilateral, the edges of etch pits of specific directions $[01\bar{1}]$, $[10\bar{1}]$ and $[\bar{1}10]$ spread over the surface at the same rate. However, in the direction normal to the (111) surface, the deepening of the etch pit will not necessarily give birth to a pyramid as the detachment of U atoms from the new exposed layer is random and not constrained at the apex of the pit. Thus, triangular etch pits with a flat bottom could be formed whose edges move outwards (as depicted by the yellow arrows in **Fig. 10(d)**). This scenario would explain the shape of the etch pits observed at different scales (**Fig. 9(b)** and **Fig. 5(c3)**). At larger scale and progress of dissolution, the large triangular etch pits had flat bottom and their edges were made of steps gradually moving away from the center. The motion of steps at the edges of triangular etch pits was thus favored compared to the digging of the pits in the direction normal to the (111) surface.

This observation led to the conclusion that the formation and growth of triangular etch pits was the predominant dissolution mechanism, which controlled the kinetics of dissolution of the (111) oriented surface of UO_2 during the induction period. The specific dissolution features observed by AFM and SEM were attributed to a dominant step-wave mechanism that ultimately led to surface-normal retreat [54].

(111) oriented surface dissolution under controlled catalysed conditions

Catalytic species produced at the solid/solution interface during the first step of UO_2 dissolution in nitric acid solution were expected to play an important role on the dissolution mechanism and dissolution rate during the second step. In order to confirm this role, a specific dissolution test was performed on (111)- ② single crystal at room temperature in 2 $mol.L^{-1}$ HNO_3 solution previously loaded with catalytic species. The evolution of the concentration of catalytic species was monitored by measuring the concentration of nitrous acid with the Griess method. In order to correct the geometric surface area, we assumed that the *Sdr* value obtained for the dissolution of (111)- ① single crystal in standard conditions was equal to that obtained for the same reaction progress in controlled catalytic conditions. The evolution of the normalized weight loss $N_L^{corr}(t)$ was then evaluated (**Fig.11 (a)**).

The analysis of the results reported in **Fig. 11(a)** shows that the concentration of HNO_2 decreased slowly from 1.7×10^{-2} to 1.3×10^{-2} mol.L^{-1} during the dissolution test, with no impact on the rate of uranium release in solution. We assumed that the catalytic species in solution resulting from the dissolution of copper chips were present in a large excess during the dissolution test of the UO_2 single crystal. Furthermore, comparison with the experiment performed in pure 2 mol.L^{-1} HNO_3 showed that the induction period (step 1) completely disappeared under controlled catalytic conditions. The normalized dissolution rate was found to be high and constant during the catalysed experiment. The linear increase of the normalized mass loss indicated that steady conditions were established. The normalized dissolution rate R_L^{corr} (g.m^{-2}.d^{-1}) and the normal retreat rate R_R^{corr} (nm.d^{-1}) were 39.5 ± 0.8 g.m^{-2}.d^{-1} and 3.6 ± 0.1 µm.d^{-1}, respectively. The R_L^{corr} value determined in catalysed conditions was found to be of the same order of magnitude than the $R_{L,2}^{corr}$ value (i.e. 10.7 ± 0.1 g.m^{-2}.d^{-1}, **Table 2**) by dissolving the (111) surface in standard conditions. This result confirmed that the second regime observed in standard conditions was kinetically controlled by the catalysed mechanism, and that the catalytic species were produced during the first kinetic step. Using the expression proposed by Charlier et al. [14], the normalized dissolution rate of UO_2 powder under catalysed conditions was evaluated to 238 g.m^{-2}.d^{-1} (i.e. 6 times higher than the value obtained for (111)-② single crystal). Once again, this comparison suggest the role of the density of defects on the dissolution rate.

At the end of the dissolution test performed under catalysed conditions (i.e. 4 days), the dissolved thickness and the mass loss equaled 15.0 ± 0.8 µm and 2.6 ± 0.1 mg, respectively. These values were close to those obtained after 35 days without adding catalytic species to the 2 mol.L^{-1} HNO_3 solution (**Table 2**). The SEM-SE micrograph of the surface of the (111)-② sample at the end of the dissolution test is presented in **Fig. 11(b)**. The dissolution of the (111) surface under catalysed conditions led to the formation, growth and coalescence of triangular etch pits. The topographic evolution of the (111) surface was found to be similar to the one obtained under standard conditions (**Fig. 5(c)**), but the time required to reach similar dissolution features was significantly reduced. This observation led again to the conclusion that the formation of triangular etch pits was related to the structure of the material at the lattice scale. It did not specifically depend on the nature of the reactive species at the UO_2/HNO_3 interface. However, the oxidative power of the reactive species with respect to U(IV) surely affected the kinetics of etch pits nucleation and growth.

4.2. Discussion

The dissolution of UO_2 oriented single crystals in nitric acid allowed us to determine reliable dissolution rates and to evidence the potential role of the crystallographic orientation. Moreover, thanks to the simplest shape of single crystals, it was easier to manage hydrodynamics in order to determine dissolution rates controlled by chemical reaction rather than by transport phenomena.

The dissolution tests of UO_2 polished single crystals in 2 $mol.L^{-1}$ HNO_3 at room temperature showed two different kinetic steps, which appeared in agreement with the literature regarding the dissolution of UO_2 in nitric acid solution. In such conditions, the speciation of nitrogen species evolved, which led to a change of the dissolution mechanism.

Mechanism occurring during the first kinetic regime

The first stage, called "induction period" occurred for $\Delta m(t) \leq 1.6 \times 10^{-5}$ g and $C_U(t) \leq 3.5 \times 10^{-7}$ $mol.L^{-1}$, i.e. for a dissolution time lower than 16 days. The results obtained in this study were in good agreement with the dissolution rates reported by Cordara et al. [21] for dense UO_2 pellets ($R_L^{corr}(U)$ and $R_R^{corr}(U)$ of 6.0×10^{-2} $g.m^{-2}.d^{-1}$ and 5.5×10^{-3} $\mu m.d^{-1}$, respectively), but were one order of magnitude lower than those published by Marc et al. [13] for UO_2 powder. Based on the results obtained in this work, such a discrepancy was attributed to the impact of the density of defects.

Indeed, extended defects were evidenced before dissolution by SEM/ECCI and AFM at the surface of the three oriented faces of UO_2 single crystals. Specific dissolution tests was performed for the (111) oriented surface in 2 $mol.L^{-1}$ HNO_3 at room temperature. A topographic evolution of the (111) surface was evidenced by AFM during the first kinetic regime. Regardless of the nature of the extended defects (dislocation loops, edge or screw dislocations), triangular etch pits opened up systematically in their vicinity. The BCF (Burton, Cabrera and Frank) theory [55] explained the growth of facets with the help of screw dislocations. A screw dislocation is a dislocation with a component of the displacement vector (Burgers vector) normal to the crystal surface. A step is generated from the end of the screw dislocation and forms a spiral in supersaturated conditions as a result of its progress. It results in a growth pyramid. Since BCF theory, some authors assumed that screw or line dislocations led to the formation of expanding etch pits during dissolution, i.e. in undersaturated conditions [23, 53, 56]. For several ubiquitous mineral phases, Lasaga and Blum [57] even determined a critical Gibbs free energy above which dislocation could become a etch pit far from equilibrium. Thus, defects constituted starting points for the topographic evolution of the surface. Even if this assumption was often made in the past, it was demonstrated experimentally in this work for the first time for UO_2. It is noteworthy that one of the key properties of the UO_2 structure is

its ability to accommodate an excess of O atoms. UO_2 fluorite structure is maintained for hyper-stoechiometric UO_{2+x} until x = 0.25 and O atoms in excess occupy the available interstitial sites. As the degree of non-stoichiometry increases, isolated interstitial defects interact with each other to create extended defect structures [58]. The number and the dynamics of these interstitial defects control macroscopic properties of the material such as the corrosion behavior. Indeed, the electrochemical reactivity of UO_{2+x} was studied by He et al. using scanning electrochemical microscopy associated to Raman spectroscopy and micro X-Ray diffraction [59-61]. They confirmed that the stoichiometry of UO_{2+x} influences significantly the surface reactivity. They also demonstrated the spatial heterogeneity of the electrochemical reactivity of UO_{2+x} and made the link between the defect structures and the reactivity. The nature of the extended defects observed at the surface of UO_2 single crystals in this work was not identified, but these structures could be linked to the presence of interstitial O atoms. These observations indicate also that the role of O_2(aq) in the nitric acid solution cannot be neglected, especially during the first kinetic stage of the dissolution. The concentration of dissolved O_2 in a 2 $mol.L^{-1}$ HNO_3 solution in equilibrium with air (i.e. for pO_2 = 0.2) is 4.1 $mmol.L^{-1}$. Even if it is much lower than the concentration of nitrate ions, O_2(aq) could act as a possible stimulant for corrosion in nitric acid during the induction period, i.e. in absence of significant amount of catalytic species, by introducing U(V) within the UO_{2+x} lattice at the solid/solution interface. The growing surface density of these U(V) sites during the first kinetic stage could increase the electronic conductivity of the surface, which could favor the reduction of nitrate ions and ultimately the production of the catalytic species. Similarly, Goldik et al. [62, 63] showed that a mixed U(IV)/U(V) UO_{2+x} surface layer catalyzed the decomposition of radiolytic H_2O_2 in alkaline media.

For the (100) and (110) surfaces, the evolution of the solid/solution interface was not observed during the first kinetic step. Thus, even if the presence of extended defects randomly distributed at the (100) and (110) surfaces was evidenced, their role during the first dissolution step was not established. Nevertheless, different starting crystallographic orientations led to different types of topography while dissolution proceeded. The mechanisms responsible for the development of specific dissolution features on (100) and (110) surfaces of UO_2 are still not elucidated. One explanation could rely on the development of surface segments with orientations that dissolved at a slower rate. For CaF_2, Godinho et al. [26, 27, 64] showed that the planes containing either Ca or F were preferentially dissolved. Thus, families of less stable surfaces tended to disappear while dissolution proceeded and the proportion of more stable surface segments increased. With time, this mechanism led to the development of a “steady topography”. Rennie et al. [29], who investigated the influence of surface orientation on the corrosion rate for UO_2 thin films, observed that while the (001) and (110) surfaces continued

to corrode at constant rate, the corrosion of the (111) stopped. Moreover, (111) surface is expected to be the most durable orientation in the UO_2 structure [65]. Indeed, calculations of the surface energy for each oriented surface of UO_2 showed that the (111) surface presented the lowest surface energy [66-69]. Thus, it was expected that the topography obtained at the end of dissolution experiments for the (100) and (110) faces contained a high proportion of surface segments of the (111) family. This assumption would explain also why the macroscopic dissolution rates determined in this work were not strongly influenced by the initial crystallographic orientation of the surface.

Mechanism occurring during the second kinetic regime

During the second step, the dissolution rate for all oriented surfaces strongly increased. Dissolution rates $R_{L,2}^{corr}$ of the (100) and (110) oriented surfaces were slightly higher than $R_{L,2}^{corr}$ of (111) oriented surface. Thus, the impact of the initial orientation on the macroscopic dissolution rate in the second kinetic step was low.

For (111) surface dissolved in the presence of catalytic species produced by copper dissolution in a 2 $mol.L^{-1}$ nitric acid solution, a unique kinetic regime was observed associated with high dissolution rate similar to $R_{L,2}^{corr}$. Thus, the presence of the species produced during copper dissolution induced a strong increase of the UO_2 dissolution kinetics. This result confirmed that the second regime observed in standard conditions was kinetically controlled by the catalysed dissolution mechanism, and that the catalytic species are produced during the first kinetic step.

At the end of the dissolution experiment in controlled catalysed conditions, (111) single crystal surface was covered by triangular etch pits. The etch pits were bigger than those observed in standard conditions, but their morphology was similar. Thus, the mechanism of nucleation and growth of triangular etch pits did not depend on the nature of the oxidant of U(IV), whether present in the nitric acid medium or formed at the UO_2/solution interface during the first step. However, the oxidative power of the reactive species in the dissolution medium could control the kinetics of etch pits nucleation and growth. As this kind of mechanism was also observed for acid-catalysed dissolution of the isostructural CaF_2, we assumed that the formation of triangular etch pits did not result from redox reaction, but rather revealed a structural control of the topographic evolution at the atomic level.

5. Conclusion

For the first time, dissolution experiments were conducted in nitric acid solution using oriented UO_2 single crystals. The single crystal/solution interface was initially free from

topographic defects, thus was considered as a geometric model. The use of polished single crystals allowed to manage properly the hydrodynamics and to avoid the establishment of concentration gradients at the solid/solution interface. Thus, the concentrations of reactive species measured in the bulk solution became representative of the solid/solution interface. Reliable dissolution rate were determined. Hence, these samples allowed to build reliable multiparametric expressions of the dissolution rate either under uncatalysed and well-controlled catalysed conditions.

This study on such oriented single crystals underlined the link between the atomic description of the UO_2 surface and the macroscopic behaviour of a sample. At the atomic scale, the enhanced reactivity of the surface located at defect sites was demonstrated. Consequently, the density of defects should be considered as a first order parameter to improve our estimation of the dissolution rates at the macroscopic scale. Beyond the measurement of the specific surface area, the next challenge to improve our estimates of SNF dissolution rates will be to take into account structural parameters in chemical engineering models of dissolution.

Acknowledgments

Authors acknowledge Béatrice Baus-Lagarde and Bruno Corso at ICSM for the technical support during ICP-MS and XRD analyzes, respectively. Authors acknowledge Adel Mesbah for fruitful discussion in the interpretation of XRD data.

Author statement

Solène Bertolotto: Conceptualization; Data curation; Formal analysis Investigation; Methodology, Writing - original draft. **Stéphanie Szenknect**: Conceptualization; Supervision; Validation; Writing - original draft; Writing - review & editing. **Sophie Lalleman:** Conceptualization; Validation; Supervision; Writing - review & editing. **Alastair Magnaldo:** Conceptualization; Formal Analysis; Validation; Writing - review & editing. **Philippe Raison:** Investigation; Methodology, Writing - review & editing. **Michael Odorico:** Investigation; Methodology; Data curation. **Renaud Podor:** Investigation; Methodology. **Laurent Claparede**: Supervision. **Nicolas Dacheux:** Conceptualization; Validation; Supervision; Writing - review & editing.

Data availability

The raw/processed data required to reproduce these findings cannot be shared at this time due to technical or time limitations.
The raw/processed data will be made available on request.

Declaration of interests

The authors declare that they have no known competing financial interests or personal relationships that could have appeared to influence the work reported in this paper.

References

[1] P.C. Burns, R.C. Ewing, A. Navrotsky, Nuclear Fuel in a Reactor Accident, Science, 335 (2012) 1184-1188.

[2] R.C. Ewing, Long-term storage of spent nuclear fuel, Nature Materials, 14 (2015) 252-257.

[3] R.J.M. Konings, T. Wiss, O. Benes, Predicting material release during a nuclear reactor accident, Nature Materials, 14 (2015) 247-252.

[4] H. Kleykamp, J.O. Paschoal, R. Pejsa, F. Thummler, Composition and structure of fission-product precipitates in irradiated oxide fuels - correlation with phase studies in the Mo-Ru-Rh-Pd and BaO-UO_2-ZrO_2-MoO_2 systems, Journal of Nuclear Materials, 130 (1985) 426-433.

[5] Y. Ikeda, Y. Yasuike, Y. Takashima, Y.Y. Park, Y. Asano, H. Tomiyasu, O-17 NMR-study on dissolution reaction of UO_2 in nitric-acid - mechanism of electron-transfer, Journal of Nuclear Science and Technology, 30 (1993) 962-964.

[6] A. Inoue, Mechanism of the oxidative dissolution of UO_2 in HNO_3 solution, Journal of Nuclear Materials, 138 (1986) 152-154.

[7] M. Shabbir, R.G. Robins, Kinetics of dissolution of uranium dioxide in nitric acid, Journal of Applied Chemistry, 18 (1968) 129.

[8] R.F. Taylor, E.W. Sharratt, L.E.M. De Chazal, D.H. Logsdail, Dissolution rates of uranium dioxide sintered pellets in nitric acid systems, Journal of Applied Chemistry, 13 (1963) 32-40.

[9] T. Fukasawa, Y. Ozawa, F. Kawamura, Generation and decomposition behavior of nitrous-acid during dissolution of UO_2 pellets by nitric-acid, Nuclear Technology, 94 (1991) 108-113.

[10] Y. Ikeda, Y. Yasuike, K. Nishimura, S. Hasegawa, Y. Takashima, Kinetic-study on dissolution of UO_2 powders in nitric-acid, Journal of Nuclear Materials, 224 (1995) 266-272.

[11] N. Desigan, N.P. Bhatt, N.K. Pandey, U.K. Mudali, R. Natarajan, J.B. Joshi, Mechanism of dissolution of nuclear fuel in nitric acid relevant to nuclear fuel reprocessing, Journal of Radioanalytical and Nuclear Chemistry, 312 (2017) 141-149.

[12] T. Dalger, S. Szenknect, F. Tocino, L. Claparede, A. Mesbah, P. Moisy, N. Dacheux, Kinetics of dissolution of $Th_{0.25}U_{0.75}O_2$ sintered pellets in various acidic conditions, Journal of Nuclear Materials, 510 (2018) 109-122.

[13] P. Marc, A. Magnaldo, J. Godard, É. Schaer, A method for phenomenological and chemical kinetics study of autocatalytic reactive dissolution by optical microscopy. The case of uranium dioxide dissolution in nitric acid media, EPJ Nuclear Sciences & Technologies, 4 (2018) 2.

[14] F. Charlier, D. Canion, A. Gravinese, A. Magnaldo, S. Lalleman, G. Borda, É. Schaer, Formalization of the kinetics for autocatalytic dissolutions. Focus on the dissolution of uranium dioxide in nitric medium, EPJ Nuclear Sciences & Technologies, 3 (2017) 26.

[15] O.N. Pogorelko, O.A. Ustinov, Effect of urea on the dissolution of U, UO_2, and U_3O_8 in concentrated HNO_3 and on the release of nitrogen-oxides, Radiochemistry, 35 (1993) 182-186.

[16] K. Nishimura, T. Chikazawa, S. Hasegawa, H. Tanaka, Y. Ikeda, Y. Yasuike, Y. Takashima, Effect of nitrous-acid on dissolution of UO_2 powders in nitric-acid optimal conditions for dissolving UO_2, Journal of Nuclear Science and Technology, 32 (1995) 157-159.

[17] C. Delwaulle, A. Magnaldo, A. Salvatores, E. Schaer, J.-L. Houzelot, B. Rodier, E. Bosse, Development of a new method for investigating the mechanisms of solid particle dissolution in nitric acid media: Millifluidic study using fluorescent indicators, Chemical Engineering Journal, 174 (2011) 383-389.

[18] P. Marc, A. Magnaldo, A. Vaudano, T. Delahaye, É. Schaer, Dissolution of uranium dioxide in nitric acid media: what do we know?, EPJ Nuclear Sciences & Technologies, 3 (2017) 13.

[19] F. Charlier, Réactions autocatalytiques hétérogènes : vers le dimensionnement des réacteurs industriels de dissolution du dioxyde d'uranium. Thèse de l'Université de Lorraine, (2017).

[20] A.L. Uriarte, R.H. Rainey, Dissolution of high-density UO_2, PuO_2 and UO_2-PuO_2 pellets in inorganic acids, ORNL-3695 (1965), pp. 81.

[21] T. Cordara, S. Szenknect, L. Claparede, R. Podor, A. Mesbah, C. Lavalette, N. Dacheux, Kinetics of dissolution of UO_2 in nitric acid solutions: A multiparametric study of the non-catalysed reaction, Journal of Nuclear Materials, 496 (2017) 251-264.
[22] C.L. Corkhill, D.J. Bailey, F.Y. Tocino, M.C. Stennett, J.A. Miller, J.L. Provis, K.P. Travis, N.C. Hyatt, Role of Microstructure and Surface Defects on the Dissolution Kinetics of CeO_2, a UO_2 Fuel Analogue, Acs Applied Materials & Interfaces, 8 (2016) 10562-10571.
[23] C.L. Corkhill, E. Myllykyla, D.J. Bailey, S.M. Thornber, J. Qi, P. Maldonado, M.C. Stennett, A. Hamilton, N.C. Hyatt, Contribution of Energetically Reactive Surface Features to the Dissolution of CeO_2 and ThO_2 Analogues for Spent Nuclear Fuel Microstructures, Acs Applied Materials & Interfaces, 6 (2014) 12279-12289.
[24] T. Fukasawa, Y. Ozawa, Relationship between dissolution rate of uranium dioxide pellets in nitric acid solutions and their porosity, Journal of Radioanalytical and Nuclear Chemistry, 106 (1986) 345-356.
[25] M. Shabbir, R.G. Robins, Effect of crystallographic orientation on dissolution of uranium dioxide in nitric acid, Journal of Nuclear Materials, 25 (1968) 236-237.
[26] J.R.A. Godinho, S. Piazolo, T. Balic-Zunic, Importance of surface structure on dissolution of fluorite: Implications for surface dynamics and dissolution rates, Geochimica Et Cosmochimica Acta, 126 (2014) 398-410.
[27] J.R.A. Godinho, S. Piazolo, L.Z. Evins, Effect of surface orientation on dissolution rates and topography of CaF_2, Geochimica Et Cosmochimica Acta, 86 (2012) 392-403.
[28] J.R.A. Godinho, C.V. Putnis, S. Piazolo, Direct Observations of the Dissolution of Fluorite Surfaces with Different Orientations, Crystal Growth & Design, 14 (2014) 69-77.
[29] S. Rennie, E.L. Bright, J.E. Sutcliffe, J.E. Darnbrough, J. Rawle, C. Nicklin, G.H. Lander, R. Springell, The Role of Crystal Orientation in the Dissolution of UO_2 Thin Films, Corrosion Science, 145 (2018) 162-169.
[30] G. Leinders, T. Cardinaels, K. Binnemans, M. Verwerft, Accurate lattice parameter measurements of stoichiometric uranium dioxide, Journal of Nuclear Materials, 459 (2015) 135-142.
[31] B.D. Cullity, Elements Of X Ray Diffraction, Addison-Wesley Publishing Company, Inc., (1956) pp.100.
[32] ISO25178-2:2012, Geometrical Product Specifications (GPS)-Surface Texture, Part 2: Terms, Definitions and Surface Texture Parameters (2012).
[33] S. Preibisch, S. Saalfeld, P. Tomancak, Globally Optimal Stitching of Tiled 3D Microscopic Image Acquisitions, Bioinformatics, 25 (2009) 1463-1465.
[34] R. Podor, X. Le Goff, T. Cordara, M. Odorico, J. Favrichon, L. Claparede, S. Szenknect, N. Dacheux, 3D-SEM height maps series to monitor materials corrosion and dissolution, Materials Characterization, 150 (2019) 220-228.
[35] D.G. Lowe, Distinctive Image Features from Scale-Invariant Keypoints, International Journal of Computer Vision, 60 (2004) 91-110.
[36] R.J. Kamaladasa, Y.N. Picard, Basic Principles and Application of Electron Channeling in a Scanning Electron Microscope for Dislocation Analysis, in: Microscopy: Science, Technology, Applications and Education, A. Méndez-Vilas and J. Díaz (Eds.), (2010) 1583-1590.
[37] H. Mansour, J. Guyon, M.A. Crimp, N. Gey, B. Beausir, N. Maloufi, Accurate electron channeling contrast analysis of dislocations in fine grained bulk materials, Scripta Materialia, 84-85 (2014) 11-14.
[38] Y.N. Picard, M. Liu, J. Lammatao, R. Kamaladasa, M. De Graef, Theory of dynamical electron channeling contrast images of near-surface crystal defects, Ultramicroscopy, 146 (2014) 71-78.
[39] M. Ben Saada, Étude du comportement visco-plastique du dioxyde d'uranium : quantification par analyse EBSD et ECCI des effets liés aux conditions de sollicitation et à la microstructure initiale. Thèse de l'Université de Lorraine, (2017).
[40] H. Kriaa, Imagerie de dislocations par contraste de canalisation des électrons : théorie et expérience. Thèse de l'Université de Lorraine, (2018).

[41] I. Gutierrez-Urrutia, S. Zaefferer, D. Raabe, Coupling of Electron Channeling with EBSD: Toward the Quantitative Characterization of Deformation Structures in the SEM, Jom, 65 (2013) 1229-1236.
[42] C. Delwaulle, Etude de La Dissolution Du Dioxyde d'uranium En Milieu Nitrique : Une Nouvelle Approche Visant à La Conpréhension Des Mécanismes Interfaciaux. Thèse de l'Institut Polytechnique de Lorraine, (2011).
[43] H. Demir, C. Ozmetin, M.M. Kocakerim, S. Yapici, M. Copur, Determination of a semi empirical kinetic model for dissolution of metallic copper particles in HNO_3 solutions, Chemical Engineering and Processing-Process Intensification, 43 (2004) 1095-1100.
[44] J. Turnbull, R. Szukalo, M. Behazin, D. Hall, D. Zagidulin, S. Ramamurthy, J.C. Wren, D.W. Shoesmith, The Effects of Cathodic Reagent Concentration and Small Solution Volumes on the Corrosion of Copper in Dilute Nitric Acid Solutions, Corrosion, 74 (2018) 326-336.
[45] J.P. Turnbull, The Influence of Radiolytically Produced Nitric Acid on the Corrosion Resistance of Copper-Coated Used Nuclear Fuel Containers, The University of Western Ontario, Electronic Thesis and Dissertation Repository. 6903, https://ir.lib.uwo.ca/etd/6903 (2020).
[46] N. Desigan, N. Bhatt, M.A. Shetty, G.K.P. Sreekumar, N.K. Pandey, U.K. Mudali, R. Natarajan, J.B. Joshi, Dissolution of nuclear materials in aqueous acid solutions, Reviews in Chemical Engineering, 35 (2019) 707-734.
[47] A. Luttge, R.S. Arvidson, C. Fischer, A Stochastic Treatment of Crystal Dissolution Kinetics, Elements, 9 (2013) 183-188.
[48] S. Homma, J. Koga, S. Matsumoto, T. Kawata, Dissolution rate-equation of UO_2 pellet, Journal of Nuclear Science and Technology, 30 (1993) 959-961.
[49] J. Cama, L. Zhang, J.M. Soler, G. De Giudici, R.S. Arvidson, A. Luttge, Fluorite dissolution at acidic pH: In situ AFM and ex situ VSI experiments and Monte Carlo simulations, Geochimica Et Cosmochimica Acta, 74 (2010) 4298-4311.
[50] L.J. Schowalter, R.W. Fathauer, R.P. Goehner, L.G. Turner, R.W. Deblois, S. Hashimoto, J.L. Peng, W.M. Gibson, J.P. Krusius, Epitaxial-growth and characterization of CaF_2 on Si, Journal of Applied Physics, 58 (1985) 302-308.
[51] C. Motzer, M. Reichling, High resolution study of etch figures on CaF2 (111), Journal of Applied Physics, 105 (2009).
[52] A. Luttge, R.S. Arvidson, Reactions at Surfaces: A New Approach Integrating Interferometry and Kinetic Simulations, Journal of the American Ceramic Society, 93 (2010) 3519-3530.
[53] A. Briggs, Dislocation etching and chemical polishing studies on UO_2 single crystals. Technical document Ref. AERE-M 859, United Kingdom Atomic Energy Authority (1961).
[54] A.C. Lasaga, A. Luttge, Variation of crystal dissolution rate based on a dissolution stepwave model, Science, 291 (2001) 2400-2404.
[55] M. Uwaha, Introduction to the BCF theory, Progress in Crystal Growth and Characterization of Materials, 62 (2016) 58-68.
[56] K. Sangwal, C.C. Desai, V. John, Etch pit morphology and calcium-sulfate growth on 111 faces of calcium-fluoride crystals etched in sulfuric-acid, Kristall Und Technik-Crystal Research and Technology, 14 (1979) 63-72.
[57] A.C. Lasaga, A.E. Blum, Surface-chemistry, etch pits and mineral-water reactions, Geochimica Et Cosmochimica Acta, 50 (1986) 2363-2379.
[58] J.W. Wang, R.C. Ewing, U. Becker, Average structure and local configuration of excess oxygen in UO_{2+x}, Scientific Reports, 4 (2014).
[59] H.M. He, Z.F. Ding, D.W. Shoesmith, The determination of electrochemical reactivity and sustainability on individual hyper-stoichiometric UO_{2+x} grains by Raman microspectroscopy and scanning electrochemical microscopy, Electrochemistry Communications, 11 (2009) 1724-1727.

[60] H.M. He, R.K. Zhu, Z. Qin, P. Keech, Z. Ding, D.W. Shoesmith, Determination of Local Corrosion Kinetics on Hyper-Stoichiometric UO_{2+x} by Scanning Electrochemical Microscopy, Journal of the Electrochemical Society, 156 (2009) C87-C94.
[61] H.M. He, D. Shoesmith, Raman spectroscopic studies of defect structures and phase transition in hyper-stoichiometric UO_{2+x}, Physical Chemistry Chemical Physics, 12 (2010) 8108-8117.
[62] J.S. Goldik, H.W. Nesbitt, J.J. Noel, D.W. Shoesmith, Surface electrochemistry of UO_2 in dilute alkaline hydrogen peroxide solutions, Electrochimica Acta, 49 (2004) 1699-1709.
[63] J.S. Goldik, J.J. Noël, D.W. Shoesmith, The electrochemical reduction of hydrogen peroxide on uranium dioxide electrodes in alkaline solution, Journal of Electroanalytical Chemistry, 582 (2005) 241-248.
[64] J.R.A. Godinho, S. Piazolo, L. Evans, Simulation of surface dynamics during dissolution as a function of the surface orientation: Implications for non-constant dissolution rates, Earth and Planetary Science Letters, 408 (2014) 163-170.
[65] P. Maldonado, J.R.A. Godinho, L.Z. Evins, P.M. Oppeneer, Ab Initio Prediction of Surface Stability of Fluorite Materials and Experimental Verification, Journal of Physical Chemistry C, 117 (2013) 6639-6650.
[66] F.N. Skomurski, R.C. Ewing, A.L. Rohl, J.D. Gale, U. Becker, Quantum mechanical vs. empirical potential modeling of uranium dioxide (UO_2) surfaces: (111), (110), and (100), American Mineralogist, 91 (2006) 1761-1772.
[67] P.W. Tasker, Surface-properties of uranium-dioxide, Surface Science, 87 (1979) 315-324.
[68] A.H.H. Tan, R.W. Grimes, S. Owens, Structures of UO_2 and PuO_2 surfaces with hydroxide coverage, Journal of Nuclear Materials, 344 (2005) 13-16.
[69] G. Sattonnay, R. Tetot, Bulk, surface and point defect properties in UO_2 from a tight-binding variable-charge model, Journal of Physics-Condensed Matter, 25 (2013).

Tables

Table 1. Sample mass (g) and geometric surface area of the oriented surface (S_{geo} in m²) determined by ImageJ software before coating and mechanical polishing. Surface texture parameters determined by AFM: average arithmetic roughness (S_a), maximum height (S_z) and developed interfacial area ratio (*Sdr*).

Sample	m (g) ± 0.001	S_{geo} (m²)	S_a (nm)	S_z (nm)	*Sdr* (%)
(100)- ①	0.212	$(1.2 \pm 0.1) \times 10^{-5}$	0.3 ± 0.1	17.8	0.05 ± 0.02
(110)- ①	0.207	$(8 \pm 1) \times 10^{-6}$	0.37 ± 0.7	28.6	0.14 ± 0.01
(111)- ①	0.240	$(1.1 \pm 0.1) \times 10^{-5}$			
(111)- ②	0.275	$(1.2 \pm 0.1) \times 10^{-5}$	0.4 ± 0.1	15.4	0.05 ± 0.01
(111)- ③*	0.021	$(7 \pm 1) \times 10^{-6}$			

** no coating*

Table 2. Elemental uranium concentration in solution C_U (mol.L^{-1}) at the end of the induction period, t_{ind}; normalized dissolution rates $R_{L,i}^{geo}$ (g.m^{-2}.d^{-1}) and normal retreat rates $R_{R,i}^{geo}$ (nm.d^{-1}) determined using the geometric surface area during the two step. Normalized dissolution rates $R_{L,2}^{corr}$ (g.m^{-2}.d^{-1}) and normal retreat rates $R_{R,2}^{corr}$ (nm.d^{-1}) determined using the corrected surface area during the second step. Elemental uranium concentration in solution C_U (mol.L^{-1}), dissolved thickness e^{corr} (µm) and dissolved mass Δm (g) at the end of experiments.

	(100)	(110)	(111)
First step with S_{geo}			
Duration t_{ind} (d)	16	14	15
$C_U(t_{ind})$ (mol.L^{-1})	(3.4 ± 0.3) × 10^{-7}	(1.7 ± 0.2) × 10^{-7}	(1.6 ± 0.2) × 10^{-7}
$R_{L,1}^{geo}$(U) (g.m^{-2}.d^{-1})	(7.4 ± 0.9) × 10^{-2}	(3.1 ± 0.5) × 10^{-2}	(3.6 ± 0.4) × 10^{-2}
$R_{R,1}^{geo}$(U) (µm.d^{-1})	(6.8 ± 0.8) × 10^{-3}	(2.9 ± 0.5) × 10^{-3}	(3.3 ± 0.4) × 10^{-3}
Second step with S_{geo}			
$R_{L,2}^{geo}$(U) (g.m^{-2}.d^{-1})	(19.6 ± 0.7)	(19.4 ± 0.8)	(13.4 ± 0.3)
$R_{R,2}^{geo}$(U) (µm.d^{-1})	(1.79 ± 0.06)	(1.77 ± 0.08)	(1.22 ± 0.03)
Second step with $S_{corr}(t)$			
$R_{L,2}^{corr}$(U) (g.m^{-2}.d^{-1})	(13.7 ± 0.6)	(14 ± 1)	(10.7 ± 0.1)
$R_{R,2}^{corr}$(U) (µm.d^{-1})	(1.25 ± 0.05)	(1.23 ± 0.09)	(0.97 ± 0.01)
End of experiment (t_f = 35 d)			
$C_U(t_f)$ (mol.L^{-1})	(4.54 ± 0.04) × 10^{-5}	(4.57 ± 0.04) × 10^{-5}	(3.94 ± 0.04) × 10^{-5}
$e^{corr}(t_f)$ (µm)	13.0 ± 0.7	20 ± 1	14.3 ± 0.7
$\Delta m(t_f)$ (g)	(2.2 ± 0.1) × 10^{-3}	(2.2 ± 0.1) × 10^{-3}	(1.9 ± 0.1) × 10^{-3}

Figure captions

Fig. 1: Crystallographic description of single crystals oriented faces, (a) lateral view, (b) top view, (c) coated samples. Figures produced using the Diamond software, where the uranium and oxygen atoms are shown in grey and red, respectively. The planes corresponding to oriented surfaces are colored.

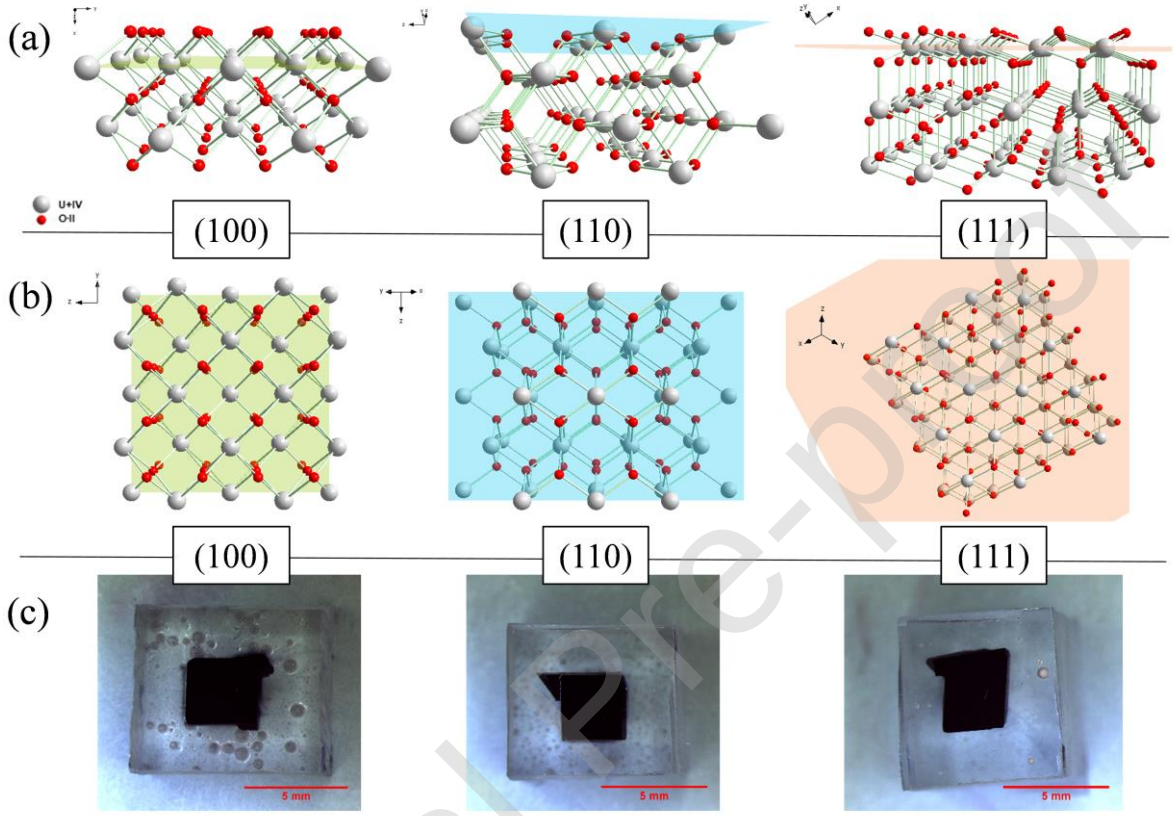

Fig. 2: XRD patterns of the three oriented faces of UO_2 single crystals after polishing: (100)-①, (110)- ① and (111)- ① samples. XRD pattern of UO_2 powdered sample used as reference (Ref).

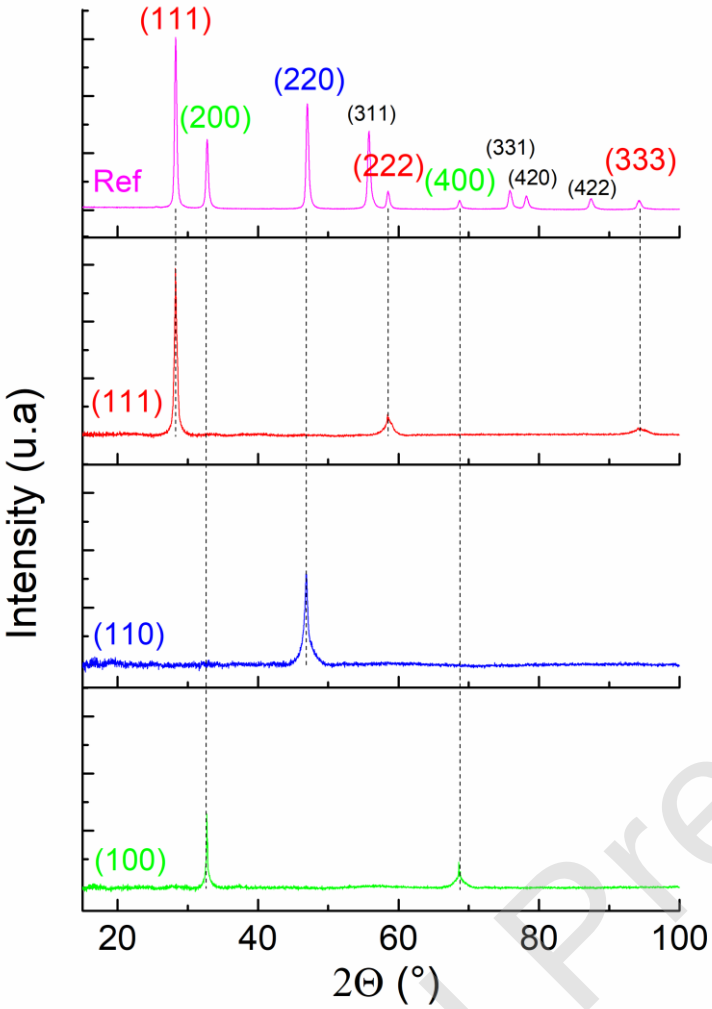

Fig. 3: Polished surface observations performed using SEM using secondary electrons (SE) detector (left) with back-scattered electrons (BSE) detector (middle) and using AFM (right). (a), (b) and (c) correspond to (100)- ①, (110)- ① and (111)- ③ samples, respectively.

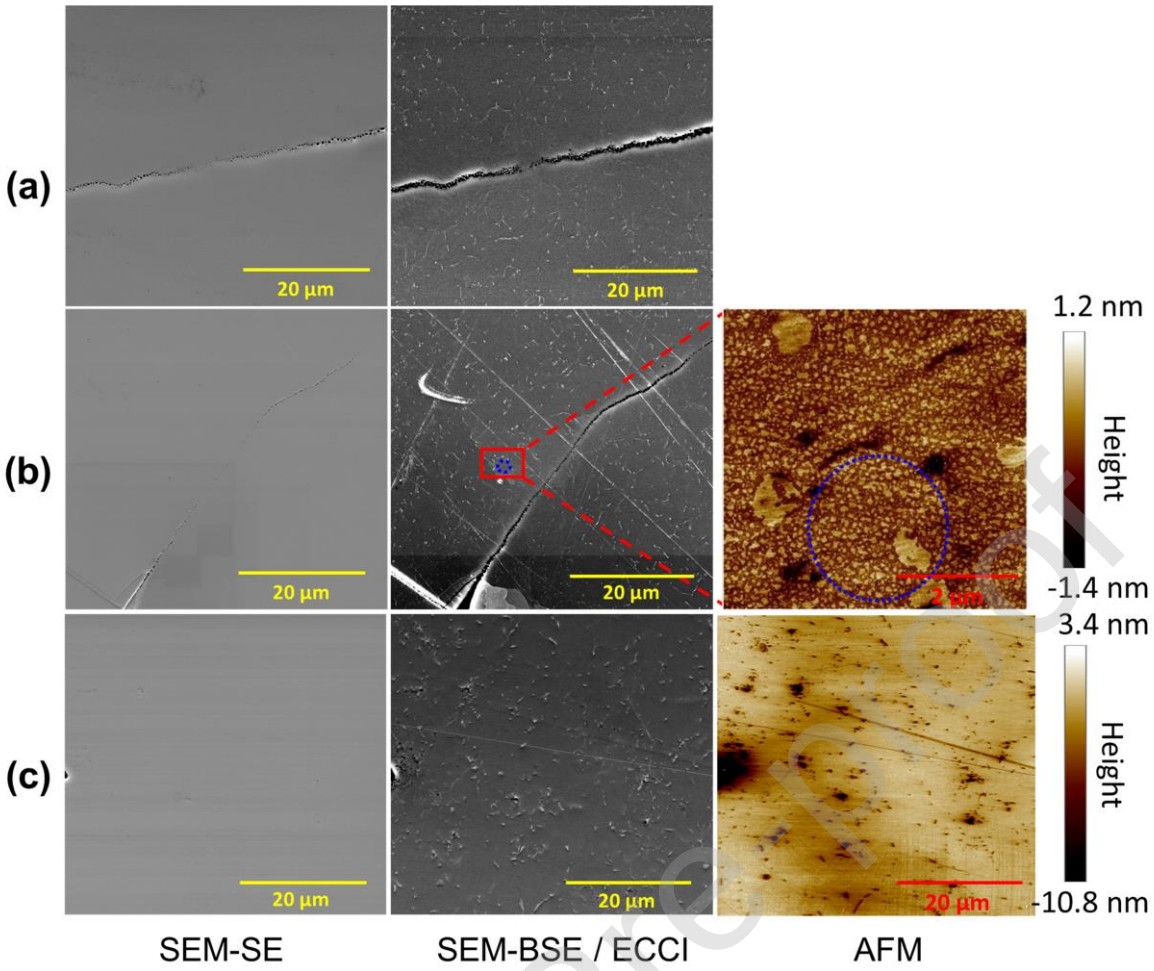

Fig. 4: Evolution of the normalized weight loss $N_L^{geo}(t)$ (left vertical axis) and of the dissolved mass $\Delta m(t)$ (right vertical axis) obtained during the dissolution in 2 mol.L^{-1} HNO_3 solution at room temperature of UO_2 oriented single crystals (a) (100)- ①; (b) (110)- ①; (c) (111)- ①.

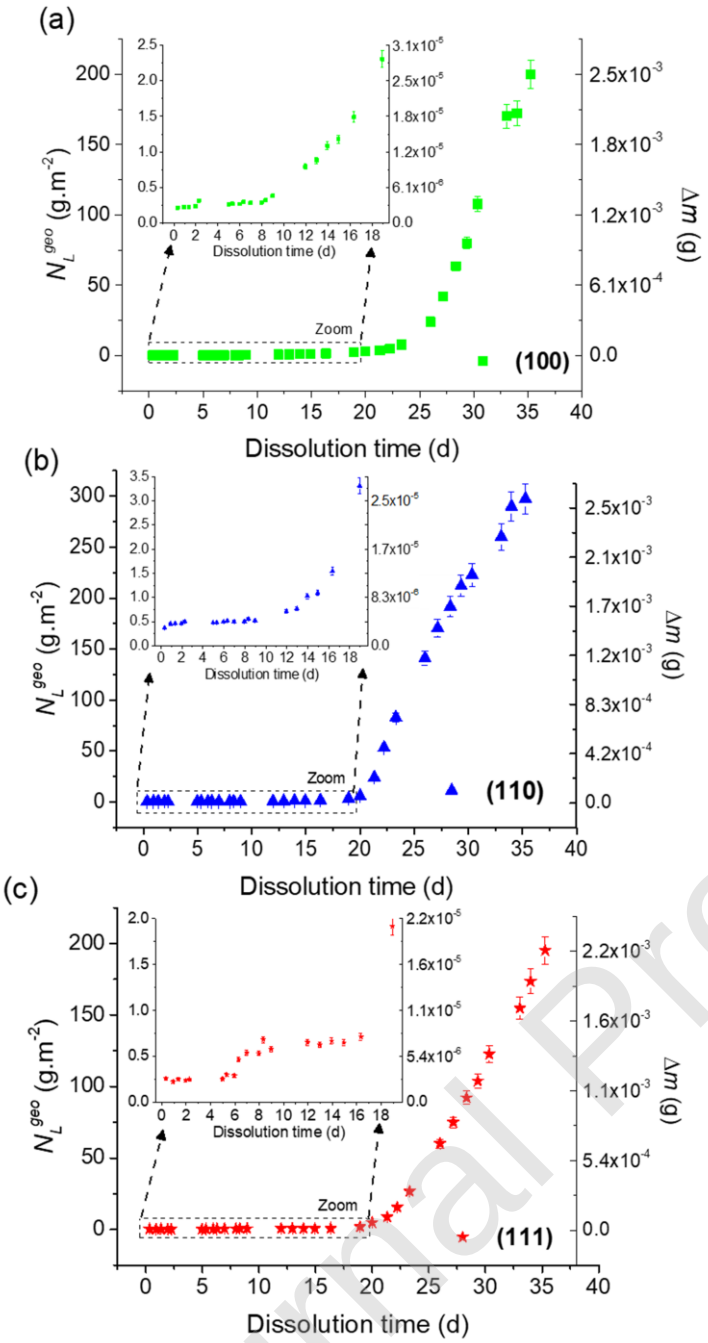

Fig. 5: Series of SEM micrographs recorded at the end of the dissolution test (35 days) for: (a) (100) surface, (b) (110) surface and (c) (111) surface at different magnifications. (1) stitching of 25 micrographs recorded at ×1,000; (2) ×2,500 micrographs; (3) ×10,000 micrographs and (4) 3D reconstructions with Mex Alicona®. The dissolved thickness determined at the end of the dissolution experiment, $e^{corr}(t_f)$ for each oriented surface is mentioned.

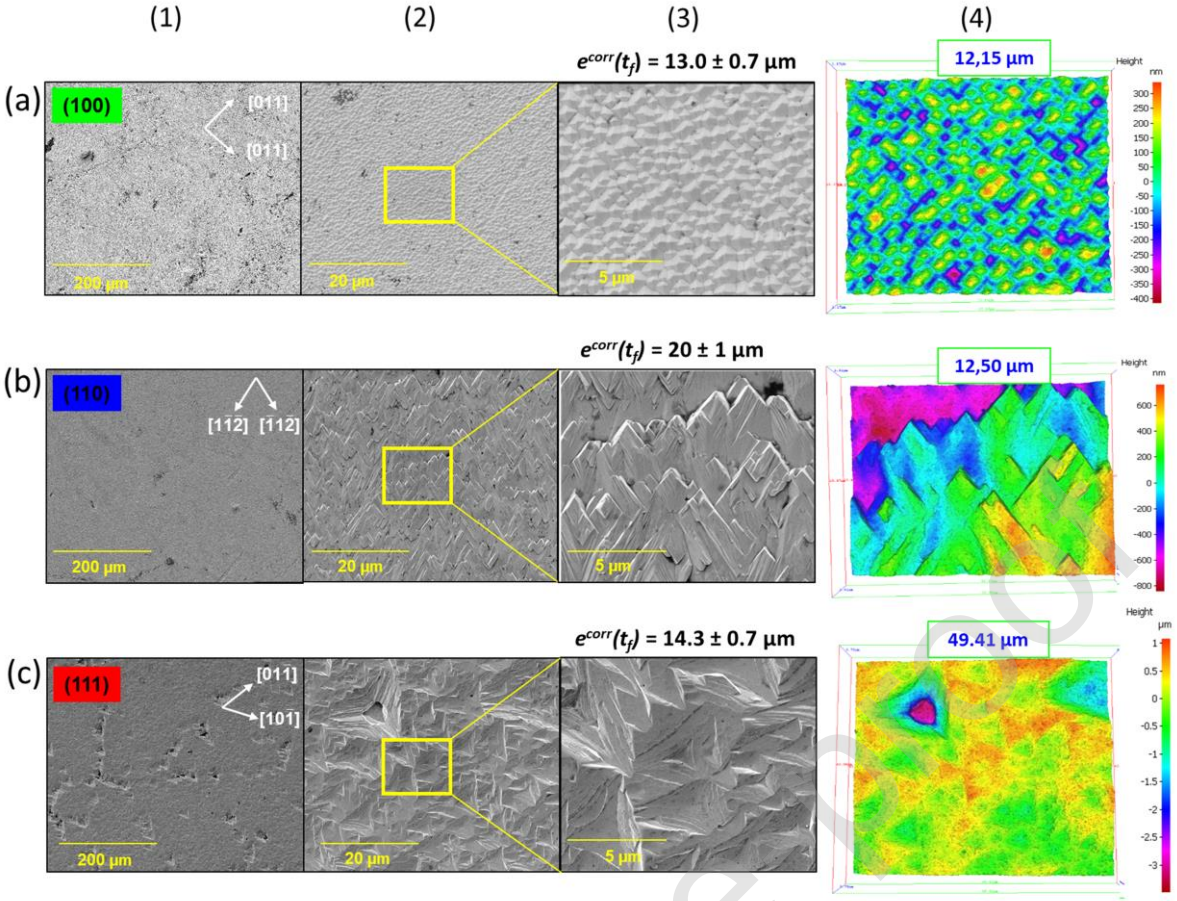

Fig. 6: Parameters calculated from 3D-reconstructions obtained with Alicona MeX® software at the end of dissolution test (35 days): developed interfacial area ratio (*Sdr*); arithmetical roughness (S_a) and maximum height (S_z).

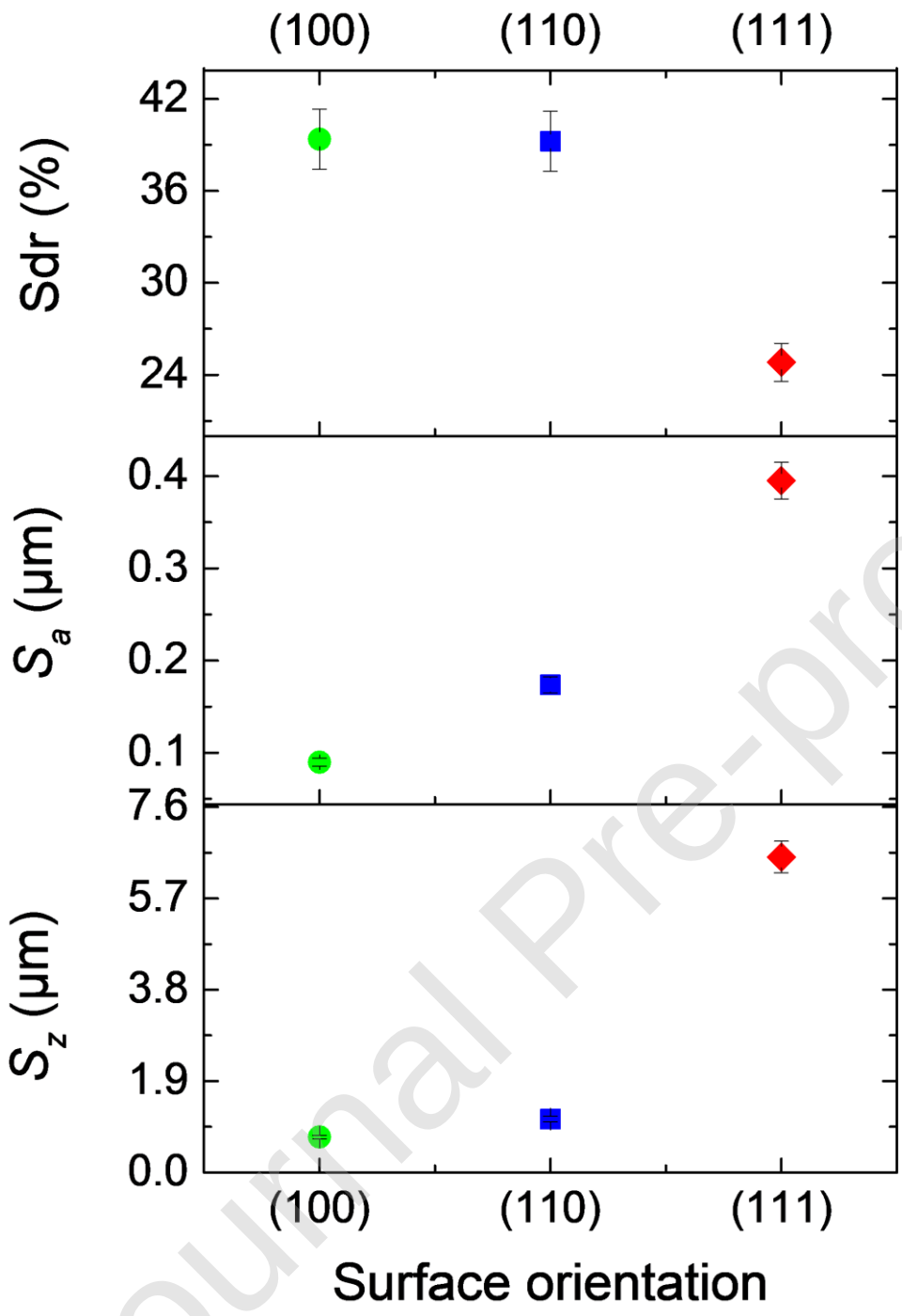

Fig. 7: Evolution of the normalized weight loss $N_L^X(t)$ (left vertical axis) and of the dissolved thickness $e^X(t)$ (right vertical axis) taking into account (a) S_{geo} and (b) $S_{corr}(t)$ for the dissolution in 2 mol.L^{-1} HNO_3 solution at room temperature of UO_2 oriented single crystals.

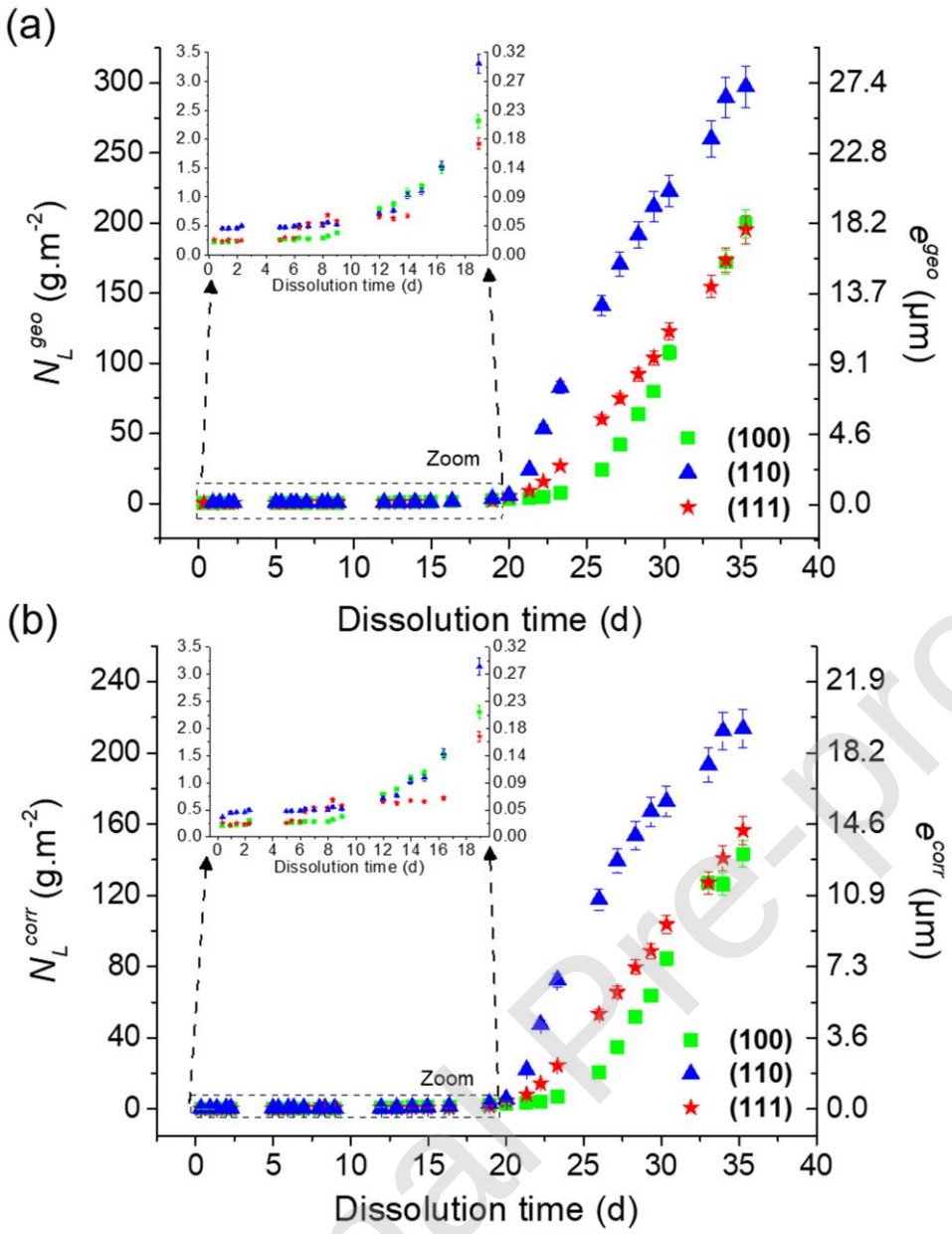

Fig. 8. AFM images of the selected ROI at the surface of (111)- ③ sample recorded at various dissolution times during the first kinetic step ($t < t_{ind}$, 2 mol.L^{-1} HNO_3, RT). Blue arrow indicates the etch pit presented in Fig.9.

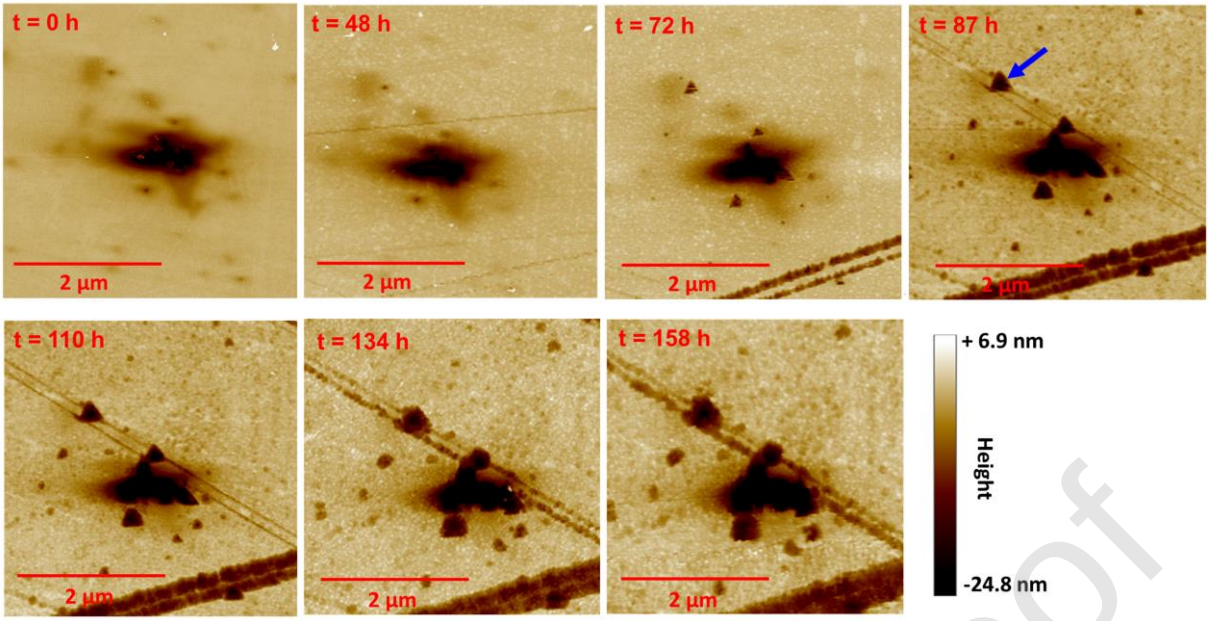

Fig. 9: Geometric details of a triangular etch pit. The blue line corresponds to the position of the depth profile drawn perpendicularly to the [$\bar{1}$10] side of the triangle (a). Evolution of the depth profile during dissolution (b).

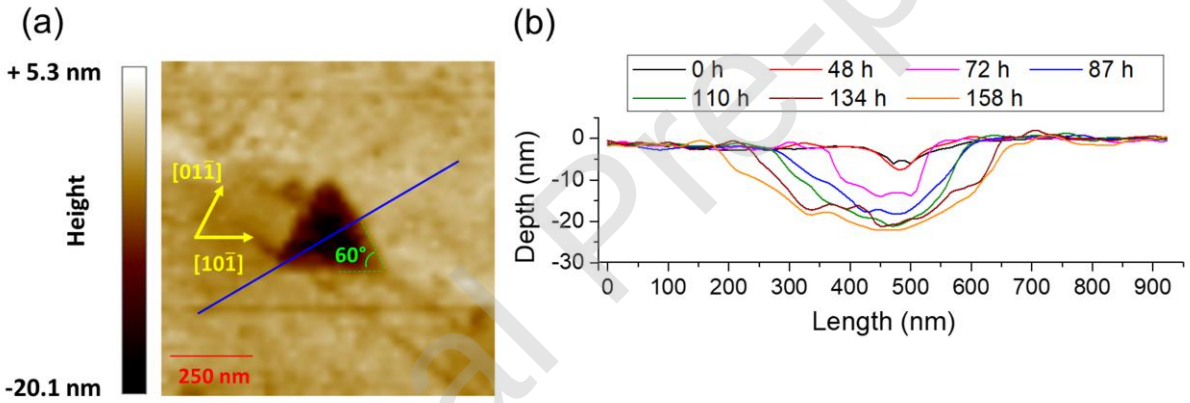

Fig. 10: Schematic illustration of the typical pit orientation on the planar (111) surface for UO_2. Uranium and oxygen atoms are respectively grey and red fill bubbles. Empty bubbles correspond to atoms pulled out from the surface: starting surface (a); random detachment of one uranium atom followed by three bridging oxygen atoms (b), detachment of a second uranium atom among the six equivalent uranium atoms surrounding the first detached atom (c) and detachment of a third uranium atom, corresponding to the only 1-coordinated atom (d), leading to the formation of the triangular pit.

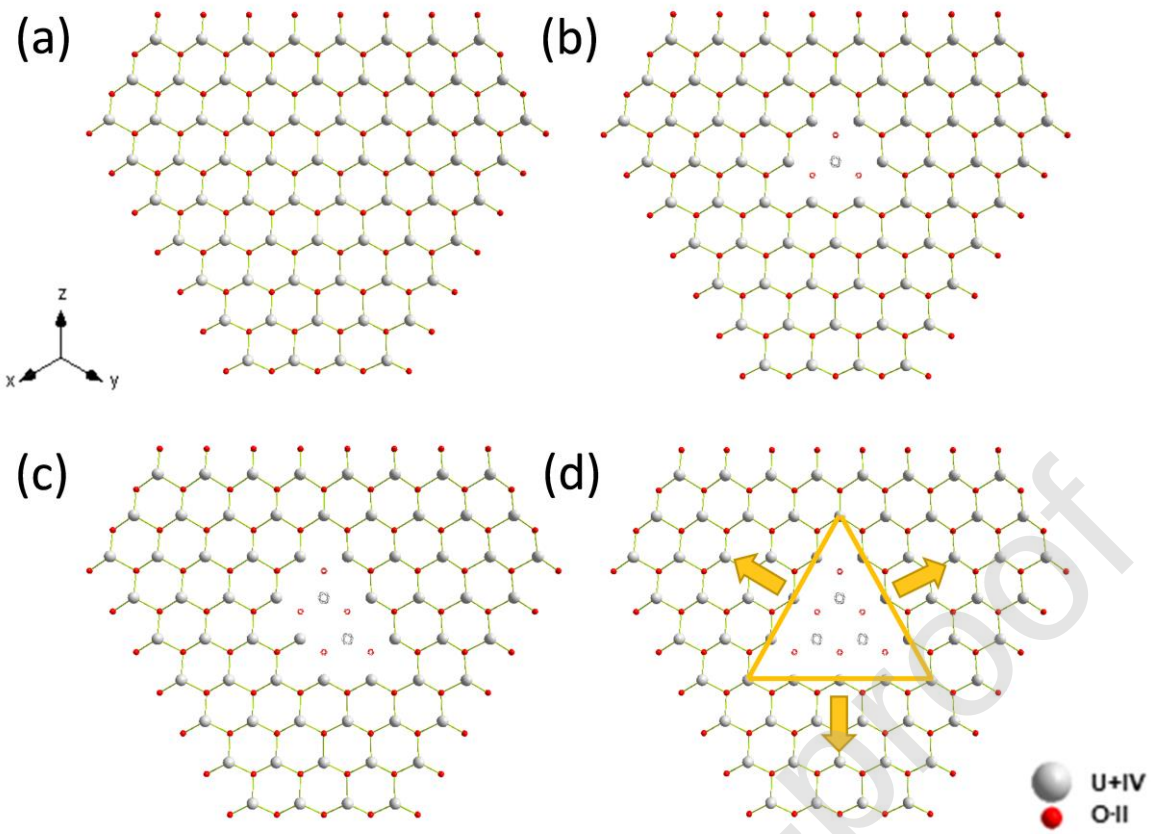

Fig. 11: (a) Evolution of the normalized weight loss $N_L^{corr}(t)$ (red stars) and of the nitrous acid concentration $C_{HNO2}(t)$ (green squares) obtained during the dissolution of (111)- ② oriented UO_2 single crystal at room temperature and in 2 mol.L^{-1} HNO_3 solution previously loaded with catalytic species. Black stars correspond to the $N_L^{corr}(t)$ values obtained in uncatalysed conditions with sample (111)- ①. (b) SEM-SE micrograph of (111) oriented surface recorded with at magnification ×2,500 at the end of the dissolution test under controlled catalytic conditions (i.e. for $e^{corr}(t_f)$ = 15.0 ± 0.8 µm).